A human ciliopathy reveals essential functions for NEK10 in airway mucociliary clearance

Raghu R. Chivukula[1,2,3,4,5*], Daniel T. Montoro[4], Hui Min Leung[6,7], Jason Yang[2,3,4,5], Hanan E. Shamseldin[8], Martin S. Taylor[2,3,4,5,9], Gerard W. Dougherty[10], Maimoona A. Zariwala[11], Johnny Carson[12], M. Leigh Anne Daniels[13], Patrick R. Sears[14], Katharine E. Black[1], Lida P. Hariri[9], Ibrahim Almogarri[15], Evgeni M. Frenkel[2,3,4,5], Vladimir Vinarsky[1], Heymut Omran[10], Michael R. Knowles[14,16], Guillermo J. Tearney[6,7,9,17], Fowzan S. Alkuraya[8*] and David M. Sabatini[2,3,4,5]

Mucociliary clearance, the physiological process by which mammalian conducting airways expel pathogens and unwanted surface materials from the respiratory tract, depends on the coordinated function of multiple specialized cell types, including basal stem cells, mucus-secreting goblet cells, motile ciliated cells, cystic fibrosis transmembrane conductance regulator (CFTR)-rich ionocytes, and immune cells[1,2]. Bronchiectasis, a syndrome of pathological airway dilation associated with impaired mucociliary clearance, may occur sporadically or as a consequence of Mendelian inheritance, for example in cystic fibrosis, primary ciliary dyskinesia (PCD), and select immunodeficiencies[3]. Previous studies have identified mutations that affect ciliary structure and nucleation in PCD[4], but the regulation of mucociliary transport remains incompletely understood, and therapeutic targets for its modulation are lacking. Here we identify a bronchiectasis syndrome caused by mutations that inactivate NIMA-related kinase 10 (NEK10), a protein kinase with previously unknown in vivo functions in mammals. Genetically modified primary human airway cultures establish NEK10 as a ciliated-cell-specific kinase whose activity regulates the motile ciliary proteome to promote ciliary length and mucociliary transport but which is dispensable for normal ciliary number, radial structure, and beat frequency. Together, these data identify a novel and likely targetable signaling axis that controls motile ciliary function in humans and has potential implications for other respiratory disorders that are characterized by impaired mucociliary clearance.

A 31-year-old consanguinous woman was evaluated for idiopathic respiratory failure characterized by neonatal respiratory distress and recurrent bacterial sinopulmonary infections (Extended Data Fig. 1a and Supplementary Table 1). Chest imaging demonstrated extensive pan-lobar bronchiectasis without heterotaxy, and nasal biopsies revealed normal ciliary radial ultrastructure (Fig. 1a,b). Cystic fibrosis and immunodeficiency were ruled out after extensive clinical and genetic testing. Similar but milder findings were present in two siblings (Extended Data Fig. 1a,b and Supplementary Table 1), strongly suggestive of autosomal recessive inheritance. Whole exome sequencing of the affected individuals unexpectedly revealed homozygous intronic splice site mutations (NM_152534:c.1230+5G>C, *NEK10*$^{G>C}$) in *NEK10*, which encodes a serine/threonine kinase homologous to *Aspergillus nidulans* NIMA (never in mitosis a) that has not been implicated previously in human disease[5] (Fig. 1c). The functions of mammalian NIMA-related kinases remain incompletely characterized. Several, including NEK2 and NEK5/6/7/9, function similarly to their fungal ortholog in cell cycle regulation through phosphorylation of centrosome components and the mitotic spindle[6]. Mutations in *NEK1* and *NEK8* cause polycystic kidney phenotypes in mice[7,8], consistent with a role in the regulation of primary cilia. Recent reports have proposed roles for NEK10 in the response of cancer cells to DNA damage[9] and in the specification of the nervous system and the body axis in teleost fish[10], but to date no published work suggests any role for NEKs in the respiratory system.

To study the effects of *NEK10*$^{G>C}$ in the lung, we isolated and cultured control and proband human bronchial epithelial cells (HBECs) obtained at the time of bilateral lung transplantation. Although *NEK10* messenger RNA was robustly expressed in airway tissue, it was essentially undetectable both in *NEK10*^{WT} and *NEK10*$^{G>C}$ HBECs, suggesting that its expression might be restricted to mature airway cells (Fig. 1d). We therefore differentiated control and patient-derived HBECs at an air–liquid interface (ALI), a well-validated method for the generation of airway epithelium in vitro[11]. Unexpectedly, both control and mutant ALI samples demonstrated robust *NEK10* mRNA expression (Fig. 1d and Extended Data Fig. 1c) despite immunoblot evidence that *NEK10*$^{G>C}$ encodes a

[1]Division of Pulmonary and Critical Care Medicine, Department of Medicine, Massachusetts General Hospital, Boston, MA, USA. [2]Whitehead Institute for Biomedical Research, Cambridge, MA, USA. [3]Howard Hughes Medical Institute, Department of Biology, Massachusetts Institute of Technology, Cambridge, MA, USA. [4]Broad Institute of Massachusetts Institute of Technology and Harvard, Cambridge, MA, USA. [5]Koch Institute for Integrative Cancer Research, Department of Biology, Massachusetts Institute of Technology, Cambridge, MA, USA. [6]Wellman Center for Photomedicine, Massachusetts General Hospital, Boston, MA, USA. [7]Harvard Medical School, Boston, MA, USA. [8]Department of Genetics, King Faisal Specialist Hospital and Research Centre, Riyadh, Saudi Arabia. [9]Department of Pathology, Massachusetts General Hospital, Boston, MA, USA. [10]Department of General Pediatrics, University Children's Hospital Muenster, Münster, Germany. [11]Department of Pathology and Laboratory Medicine, University of North Carolina at Chapel Hill, Chapel Hill, NC, USA. [12]Department of Pediatrics, University of North Carolina at Chapel Hill, Chapel Hill, NC, USA. [13]Division of Pulmonary Diseases and Critical Care Medicine, Department of Medicine, University of North Carolina at Chapel Hill, Chapel Hill, NC, USA. [14]Cystic Fibrosis/Pulmonary Research and Treatment Center, University of North Carolina at Chapel Hill, Chapel Hill, NC, USA. [15]Department of Pediatrics, King Faisal Specialist Hospital and Research Centre, Riyadh, Saudi Arabia. [16]Marsico Lung Institute, University of North Carolina at Chapel Hill, Chapel Hill, NC, USA. [17]Harvard–MIT Division of Health Sciences and Technology, Cambridge, MA, USA. *e-mail: raghu@wi.mit.edu; falkuraya@kfshrc.edu.sa

loss-of-function allele (Fig. 1e and Extended Data Fig. 1d). To elucidate the mechanism by which *NEK10*$^{G>C}$ impairs protein expression, we sequenced full-length complementary DNAs from mutant ALI samples and revealed a mutation-dependent in-frame insertion of seven amino acids, which we suspected rendered NEK10 unstable (Fig. 1f). To test this hypothesis, we expressed epitope-tagged NEK10 constructs in HEK293T cells and found, as in ALI cultures, that the mutant protein was severely under-expressed, supporting a destabilizing effect of *NEK10*$^{G>C}$ that causes loss of function (Fig. 1g).

These findings led us to ask whether *NEK10* mutations might underlie other cases of unexplained bronchiectasis. Indeed, further sequencing revealed six additional patients from four families who harbored homozygous *NEK10* mutations and exhibited bronchiectasis (Extended Data Fig. 1e–o). The first, an 11-year-old girl, had a homozygous c.1869dupT mutation that resulted in frameshift and premature stop (His624Serfs*4). The second, a 15-year-old girl, had a homozygous c.2243C>T mutation that caused substitution of a leucine for a highly conserved proline (Pro748Leu) within the kinase domain. The third, a 23-year-old woman, had a homozygous c.1373+1G>T mutation that caused exon skipping, frameshift, and premature stop (Cys437Thrfs*9). The fourth, fifth, and sixth were siblings with a homozygous c.2317C>T mutation that resulted in the replacement of a highly conserved arginine by a cysteine (Arg773Cys). Notably, clinical assays revealed normal nasal ciliary ultrastructure observed by electron microscopy, normal nasal nitric oxide levels, no evidence of heterotaxy, and only very subtle abnormalities observed by clinical high-speed video microscopy in all tested individuals, suggesting that such patients might escape detection during standard PCD evaluation[12] (Supplementary Table 1). Linkage analysis that incorporated kindreds 1–3 yielded a single, highly significant genome-wide linkage signal (pLOD 5.2), defining a 7.3 Mb interval that included the *NEK10* locus (Fig. 1h). By contrast, healthy individuals with biallelic inactivating *NEK10* mutations are completely absent from publicly available variant databases[13]. Together, these data provide strong genetic and clinical evidence that *NEK10* represents a novel and bona fide autosomal recessive bronchiectasis locus.

Given the roles of NEKs in cell cycle regulation, we initially reasoned that NEK10 is required for the specification of one or more cell types that are involved in mucociliary clearance. Quantitative PCR with reverse transcription (qRT–PCR) revealed that *NEK10* is robustly induced during airway epithelial differentiation, coincident with the acquisition of markers for ciliated and secretory cells and the depletion of stem cell markers (Extended Data Fig. 2a–d). However, *NEK10*$^{G>C}$ cultures induced and repressed these markers with kinetics identical to those of control cultures and produced similar numbers of secretory, goblet, and multiciliated cells (MCCs, Extended Data Fig. 2e,f). These data suggested that NEK10 might instead function specifically within one of the specialized cells that are important for mucociliary clearance. To characterize the *NEK10* expression domain, we generated ALI cultures in which enhanced green fluorescent protein (eGFP) is expressed under the control of the *NEK10* promoter (*NEK10*:eGFP), which we found directs expression within a subset of ALI cells in a differentiation-dependent manner (Extended Data Fig. 2g,i). GFP+ cells purified by FACS from mature *NEK10*:eGFP ALI cultures revealed a 149-fold enrichment of the MCC marker *FOXJ1* (ref. [14]) and reciprocal depletion of secretory and basal cell marker transcripts (Fig. 2a). Confocal imaging confirmed that GFP positivity was restricted to cells that harbored apical cilia (Fig. 2b). Conversely, FACS-purified ciliated cells from *FOXJ1*:eGFP ALI cultures revealed a 152-fold enrichment of *NEK10* (Extended Data Fig. 2h,i and Fig. 2a). These findings establish *NEK10* as a ciliated-cell-specific gene in the human airway that is induced during, but dispensable for, differentiation of this cell type.

To explore the functional roles of NEK10 in MCCs, we imaged live ALI cultures with high-frame-rate phase contrast microscopy and observed a striking reduction in overall ciliary motion in *NEK10*$^{G>C}$ cultures (Fig. 2c, Extended Data Fig. 3a and Supplementary Movie 1). Given this abnormality, we performed advanced MCC functional phenotyping using micro-optical coherence tomography (μOCT), a state-of-the-art high-resolution live imaging technique capable of quantitatively interrogating multiple ciliary parameters[15]. Unlike control cultures that robustly transport polystyrene beads added to the apical ALI surface, *NEK10*$^{G>C}$ ALI cultures showed a near-absence of mucociliary transport (MCT) (Fig. 2d, Extended Data Fig. 3b and Supplementary Movie 2) and a reduction in the depth of the periciliary liquid layer (PCL, Fig. 2e). We were surprised to measure normal ciliary beat frequency in mutant ALI cultures (Extended Data Fig. 3c), again suggesting a mode of dysfunction distinct from that of classical PCD. Although these data suggest a causative role for *NEK10* loss of function in MCC dysfunction, they do not rule out the possibility that secondary genetic or acquired changes in proband-derived cells were responsible[16]. We therefore generated CRISPR–Cas9-mediated NEK10 loss-of-function ALI cultures (*NEK10*^{KO}) by genetically disrupting the *NEK10* locus in wild-type HBECs. Immunoblotting confirmed the efficient depletion of NEK10, and live microscopy of *NEK10*^{KO} ALI cultures revealed a dramatic reduction in ciliary motion, as observed in *NEK10*$^{G>C}$(Fig. 2f and Extended Data Fig. 3d,e). We also subjected *NEK10*^{KO} ALI cultures to μOCT imaging and found a severe reduction in maximal particle transport velocity and a thinning of the PCL, again without a change in ciliary beat frequency (CBF) (Fig. 2g,h and Extended Data Fig. 3f).

Given a recent report of catalysis-independent roles for NEKs[17], we sought to understand whether kinase activity per se is necessary for NEK10 function in MCCs. We therefore generated *NEK10*$^{G>C}$

Fig. 1 | Familial bronchiectasis associated with *NEK10* loss of function. a, Chest computed tomography (CT) imaging of proband 1 upon clinical presentation. The dashed line indicates the level of the cross-sectional image in the right panel. The arrows highlight cystic bronchiectatic destruction of the lung. **b**, Transmission electron micrograph (TEM) of a nasal biopsy specimen from proband 1 that demonstrates normal radial ciliary ultrastructure. Scale bars, 100 nm. **c**, Schematic depiction of the 3′ terminus of *NEK10* exon 15 and the following intron. The Sanger sequencing traces highlight the G>C point mutation (red nucleotide) and high degree of conservation (red dashed box). **d**, 18S rRNA-normalized relative expression of the indicated amplicons. $n=3$ independent lung tissue donors (controls), $n=5$ independently isolated *NEK10*$^{G>C}$ lung regions, $n=3$ independently isolated HBEC lines for *NEK10*$^{G>C}$, and $n=1$ for all remaining samples. n.s., not significant. Mean ± s.d. **e**, Immunoblotting against the indicated proteins from cultured HBECs and ALI cultures. NEK10 immunogens are indicated. C term, C terminus. GAPDH, glyceraldehyde-3-phosphate dehydrogenase. N term, N terminus. Immunoblots are representative of three experiments. **f**, Schematic representations of *NEK10* cDNA sequencing results from two *NEK10* genotypes and homologous sequences from five species. Common residues are indicated in yellow, and *NEK10*$^{G>C}$-specific residues are indicated in red. Canonical and cryptic splice donor motifs are highlighted in black and red dashed boxes, respectively. **g**, Immunoblotting after transient transfection of HEK293T cells with the indicated cDNAs. Immunoblots are representative of two experiments. **h**, Results of genome-wide linkage analysis that incorporated the 15 individuals highlighted with asterisks in Extended Data Fig. 1a,e,g. The peak is bounded by marker SNPs rs13072262 and rs17798444, and the red line indicates an LOD of 3.3, equivalent to genome-wide $P<0.05$. Images in **c** and **f** were generated using the University of California Santa Cruz (UCSC) genome browser hg19 assembly (http://genome.ucsc.edu). WT, wild type.

ALI cultures with *FOXJ1*-promoter-driven re-expression of NEK10^{WT} or, alternatively, NEK10 variants predicted to inactivate[18] (NEK10^{K548R}) or putatively hyperactivate (NEK10^{S684D}, NEK10^{Y590A}) activity based on prior studies of paralogous NEK kinases[6,19,20]. Despite sub-physiological expression of transduced NEK10 variants, live microscopy demonstrated a striking increase in motility upon expression of NEK10^{S684D}, partial rescue with NEK10^{WT} and NEK10^{Y590A}, and no effect of catalytic-dead NEK10^{K548R} (Extended Data Fig. 3g–i). Live imaging with μOCT demonstrated that CBF was again unaffected by NEK10 status but that particle transport

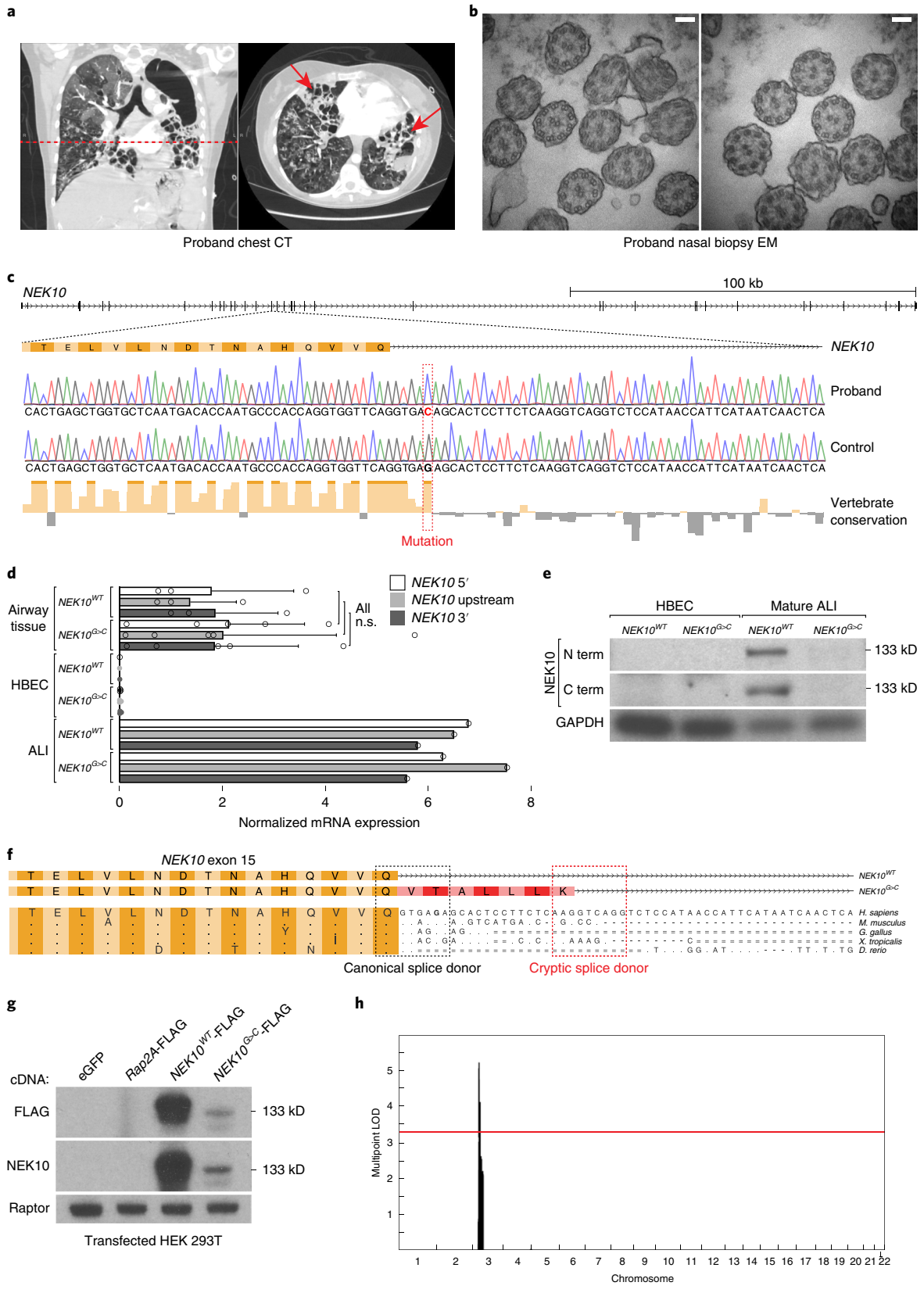

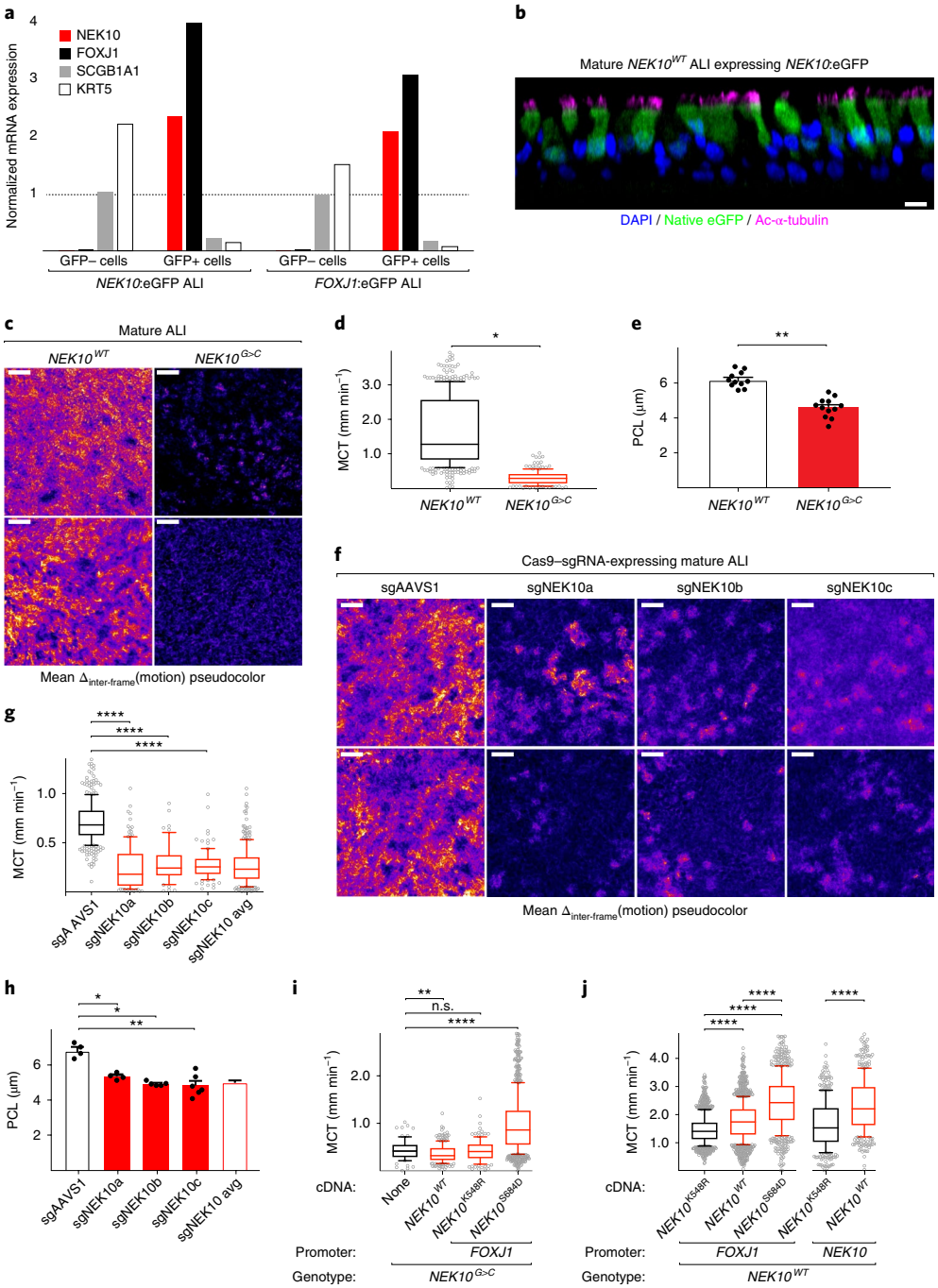

Fig. 2 | *NEK10* is a ciliated-cell-specific gene required for effective mucociliary transport. a, 18S rRNA-normalized relative expression of indicated transcripts from FACS-sorted ALI cells. The dashed line indicates the expression level from unsorted mature ALI cells. **b**, Confocal immunofluorescence demonstrating GFP expression in ciliated cells of *NEK10*:eGFP ALI cultures, representative of two independent ALI differentiations. Scale bar, 10 μm. **c**, Pseudocolored video microscopy of ALI cultures of the indicated genotypes, representative of three independent ALI differentiations. Mean Δ inter-frame (motion) pseudocolor represents motion amplitude as color intensity. Scale bars, 50 μm. **d**, MCT (μOCT) of mature ALI cultures of the indicated genotypes. The center line of the box plot indicates the median, the box bounds the 25th and 75th percentiles, the whiskers indicate the 10th and 90th percentiles, and the open circles indicate the remaining points. $n = 485$ for $NEK10^{WT}$ and $n = 180$ for $NEK10^{G>C}$, pooled from three independent ALI differentiations. **e**, PCL (μOCT) of ALI cultures of the indicated genotypes. $n = 11$ for $NEK10^{WT}$ and $n = 12$ for $NEK10^{G>C}$, pooled from three independent ALI differentiations. Mean ± s.e.m. **f**, Pseudocolored video microscopy of CRISPR–Cas9-edited ALI cultures. Images show representative fields from three independent ALI differentiations. Scale bars, 50 μm. **g**, MCT of CRISPR–Cas9-edited ALI cultures plotted as in **d**. $n = 361$, $n = 131$, $n = 59$, and $n = 104$ for sgAAVS1, sgNEK10a, sgNEK10b, and sgNEK10c, respectively, pooled from three independent ALI differentiations. **h**, PCL of CRISPR–Cas9-edited ALI cultures. $n = 4$, $n = 4$, $n = 5$, and $n = 6$ for sgAAVS1, sgNEK10a, sgNEK10b, and sgNEK10c, respectively, pooled from three independent ALI differentiations. Mean ± s.e.m. **i**, MCT of $NEK10^{G>C}$ ALI cultures expressing cDNAs encoding the indicated mutants, plotted as in **d**. $n = 71$, $n = 254$, $n = 129$, and $n = 1{,}081$ for no cDNA, $NEK10^{WT}$, $NEK10^{K548R}$, and $NEK10^{S684D}$, respectively, pooled from three independent ALI differentiations. Mean ± s.e.m. **j**, MCT of $NEK10^{WT}$ ALI cultures expressing cDNAs encoding the indicated mutants, plotted as in **d**. $n = 1{,}385$, $n = 1{,}624$, $n = 728$, $n = 401$, and $n = 426$ for $FOXJ1{:}NEK10^{K548R}$, $FOXJ1{:}NEK10^{WT}$, $FOXJ1{:}NEK10^{S684D}$, $NEK10{:}NEK10^{K548R}$, and $NEK10{:}NEK10^{WT}$, respectively, pooled from three independent ALI differentiations. WT, wild type. $^{*}P \leq 0.05$, $^{**}P \leq 0.01$, $^{****}P \leq 0.0001$.

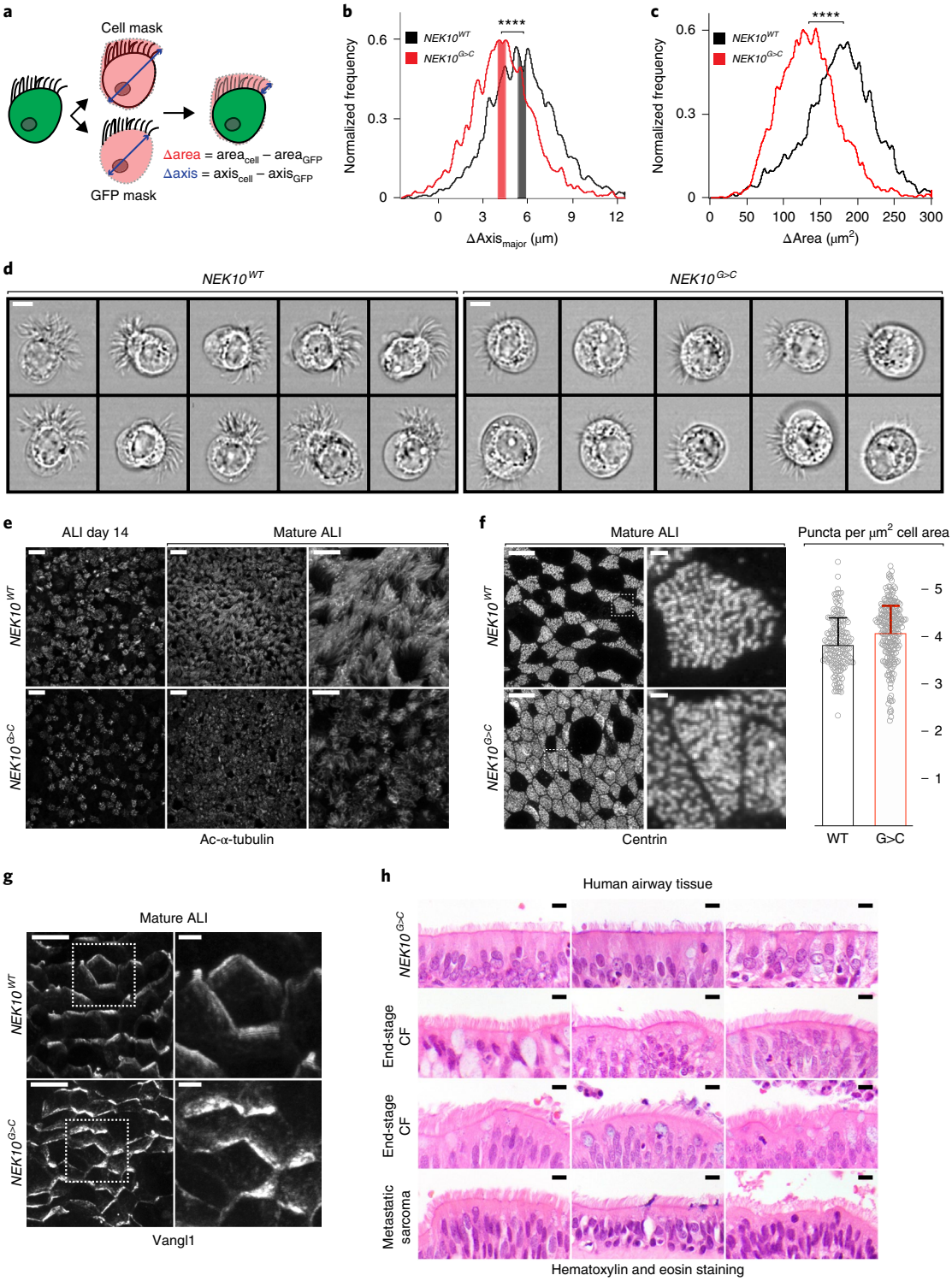

Fig. 3 | Morphologically abnormal ciliated cells in NEK10-deficient airway. a, Schematic masking workflow for IFC morphological analysis. **b**, Histogram of ciliary zone thickness in mature ALI MCCs of the indicated genotypes. $n = 4{,}108$ for $NEK10^{WT}$ and $n = 3{,}513$ for $NEK10^{G>C}$. The shaded bars indicate medians ±0.25 μm. **c**, Histogram of ciliary area in mature ALI MCCs of the indicated genotypes. $n = 4{,}108$ for $NEK10^{WT}$ and $n = 3{,}513$ for $NEK10^{G>C}$. **d**, Single cell images taken from the shaded regions in **b**. Scale bars, 7 μm. **e**, Confocal maximum intensity projections (MIPs) of ALI cultures of the indicated genotype and maturity after IFM against Ac-α-tubulin, representative of three independent ALI differentiations. Scale bars, 25 μm (left four panels) and 10 μm (right two panels). **f**, Confocal MIPs of mature ALI cultures after IFM against the basal body marker centrin. Dashed boxes mark full resolution regions shown in the middle panels. Scale bars, 10 μm (left two panels) and 1 μm (middle two panels). The column graph shows the number of centrin puncta per μm² of ciliated cell surface area. $n = 71$ cells and 10,855 puncta for $NEK10^{WT}$, and $n = 38$ cells and 5,369 puncta for $NEK10^{G>C}$, pooled from four independent ALI differentiations. Mean ± s.d. **g**, Confocal MIPs of mature ALI cultures after IFM against the PCP marker Vangl1, representative of three independent ALI differentiations. The dashed boxes mark full resolution regions shown in the right panels. Scale bars, 10 μm (left panels) and 2.5 μm (right panels). **h**, H&E stained human large airway tissue. The upper three samples were taken from lung explants during transplantation for end-stage bronchiectasis owing to the indicated etiologies, and the fourth sample was taken from a patient undergoing resection for an unrelated diagnosis. Scale bars, 5 μm. WT, wild type. $^{****}P \leq 0.0001$.

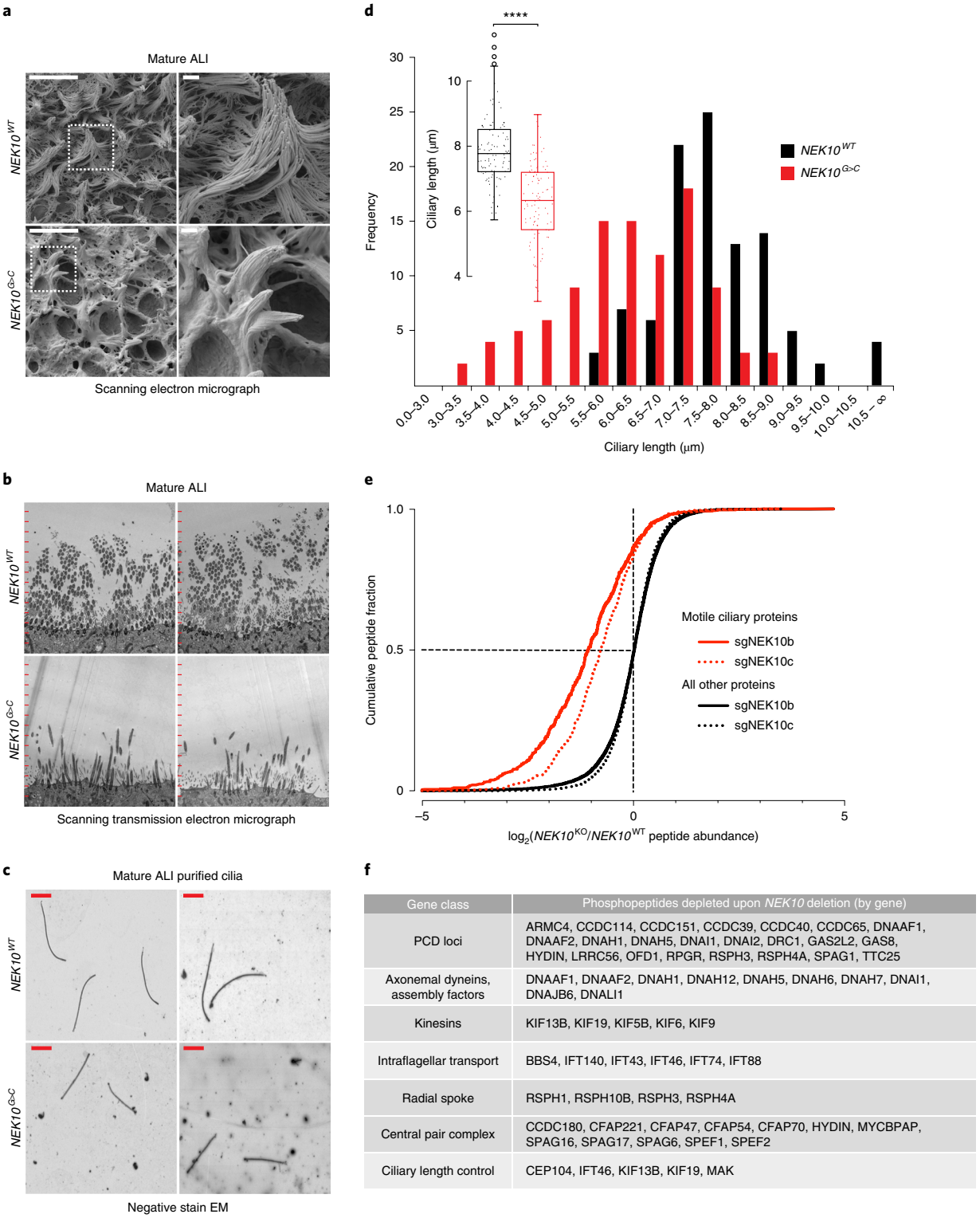

Gene class	Phosphopeptides depleted upon *NEK10* deletion (by gene)
PCD loci	ARMC4, CCDC114, CCDC151, CCDC39, CCDC40, CCDC65, DNAAF1, DNAAF2, DNAH1, DNAH5, DNAI1, DNAI2, DRC1, GAS2L2, GAS8, HYDIN, LRRC56, OFD1, RPGR, RSPH3, RSPH4A, SPAG1, TTC25
Axonemal dyneins, assembly factors	DNAAF1, DNAAF2, DNAH1, DNAH12, DNAH5, DNAH6, DNAH7, DNAI1, DNAJB6, DNALI1
Kinesins	KIF13B, KIF19, KIF5B, KIF6, KIF9
Intraflagellar transport	BBS4, IFT140, IFT43, IFT46, IFT74, IFT88
Radial spoke	RSPH1, RSPH10B, RSPH3, RSPH4A
Central pair complex	CCDC180, CFAP221, CFAP47, CFAP54, CFAP70, HYDIN, MYCBPAP, SPAG16, SPAG17, SPAG6, SPEF1, SPEF2
Ciliary length control	CEP104, IFT46, KIF13B, KIF19, MAK

Fig. 4 | NEK10 regulates ciliary length through widespread effects on the ciliary proteome. a, SEMs of mature ALI cultures of the indicated genotype, representative of three independent ALI differentiations. The dashed boxes mark full resolution regions shown in the right panels. Scale bars, 10 μm (left panels) or 1 μm (right panels). **b**, STEMs of mature ALI cultures of the indicated genotype after embedding and sectioning orthogonal to the epithelial surface, representative of three independent ALI differentiations. Tick marks are spaced at 1 μm. **c**, Representative negative stain electron microscopy grids prepared from purified cilia of the indicated genotypes, representative of two independent ALI differentiations. Scale bar, 1 μm. **d**, Histogram of ciliary length from purified cilia of the indicated genotypes. $n = 101$ for *NEK10*^{WT} and $n = 102$ for *NEK10*$^{G>C}$, pooled from two independent ALI differentiations. The inset shows a box and whisker plot of these data, in which the center line indicates the median, the box bounds the 25th and 75th percentiles, the whiskers indicate 1.5 times the interquartile range, and the circles indicate outliers. **e**, Cumulative distribution of phosphopeptides by $\log_2$[fold change]. Previously identified motile ciliary proteins are shown in red, and all other detected proteins are shown in black. sgNEK10b and sgNEK10c are independently targeting guide RNAs validated in Extended Data Fig. 3d. **f**, Table of ciliary genes by functional class showing phosphopeptides that were depleted more than twofold upon *NEK10* deletion. WT, wild type. ****$P \leq 0.0001$.

was significantly increased upon expression of NEK10^{S684D} (Fig. 2i and Extended Data Fig. 3j). These data led us to ask whether ectopic activation of NEK10 signaling in wild-type ALI cultures could augment mucociliary transport to supraphysiological levels. Indeed, expression of NEK10^{WT} or NEK10^{S684D} under the control of the *FOXJ1* promoter significantly increased transport velocity compared to catalytic-dead NEK10^{K548R}, a phenotype that was also reproduced with the more transcriptionally active *NEK10* promoter (Fig. 2j). Together, these data establish (1) that ciliated-cell-specific NEK10 kinase activity is required for effective airway mucociliary transport, (2) that NEK10 activity is constrained by the serine 684 activation loop residue, and (3) that the potentiation of NEK10 activity may represent a strategy for the augmention of mucociliary transport.

We next turned our attention to the mechanisms by which NEK10 regulates MCC function. To evaluate whether mutant MCCs harbor some physical abnormality, we used imaging flow cytometry (IFC), which enables the capture of thousands of single cells for statistically robust morphology analysis[21]. After gating singlet MCCs from *NEK10*:eGFP ALI cultures (Extended Data Fig. 4a,b), we measured per-cell ciliary area and ciliary zone thickness, revealing a clear and statistically significant reduction in both parameters in the mutant MCCs (Fig. 3a–c). Representative single cells corroborated this finding, demonstrating a hypoplastic ciliary layer in *NEK10*$^{G>C}$ MCCs (Fig. 3d). To validate this result using an orthogonal method, we subjected *NEK10*$^{G>C}$ ALI cultures to confocal immunofluorescence microscopy (IFM) against acetylated α-tubulin (Ac-α-tubulin). We again found that mutant ALI cultures harbored strikingly abnormal cilia with a hypoplastic appearance (Fig. 3e). *NEK10*^{KO} ALI cultures phenocopied this morphology, and NEK10^{S684D}-complemented *NEK10*$^{G>C}$ ALI cultures reversed it (Extended Data Fig. 4c,d), indicating that this phenotype is specifically attributable to NEK10 kinase activity. Previously described human mutations[22,23] are known to impair the nucleation and density of motile cilia. We therefore evaluated MCC basal body density by IFM but found no reduction that would account for the *NEK10*$^{G>C}$ phenotype (Fig. 3f). In light of the links between planar cell polarity (PCP) and ciliogenesis[24], we also confirmed that NEK10 activity is dispensable for MCC planar polarization (Fig. 3g). Finally, to validate ALI culture findings in human patients, we compared airway tissue from the explanted lungs of the proband with airway tissue from subjects without bronchiectasis and patients with end-stage cystic fibrosis. As in ALI cultures (Extended Data Fig. 4e), histological analysis revealed ciliary hypoplasia only in the airway of the patient with the *NEK10* mutation (Fig. 3h), indicating that this phenotype does not reflect a non-specific consequence of severe bronchiectasis and that NEK10 deficiency produces short motile cilia in vivo, a previously undescribed human genetic phenotype.

As the size of motile cilia limits their structural analysis by light microscopy, we next subjected ALI preparations to three complementary modes of electron microscopy analysis. Scanning electron microscopy (SEM) of intact ALI, like IFM, revealed that *NEK10*$^{G>C}$ and *NEK10*^{KO} ALI cultures harbor morphologically abnormal cilia of heterogeneous length with excess mucus accumulation (Fig. 4a and Extended Data Fig. 5a). Electron microscopy imaging of sectioned ALI cultures revealed a decrease in ciliary length in the *NEK10*$^{G>C}$ cultures (Fig. 4b) but did not show the undocked centrioles seen in ciliary aplasia syndromes or the ciliary tip 'ballooning' reported with certain intraflagellar transport defects[22,23]. To quantify this length defect precisely, we biochemically isolated axonemes from ALI cultures[25] (Extended Data Fig. 5b) and subjected these preparations to negative stain electron microscopy followed by measurement of individual cilia. Isolated *NEK10*$^{G>C}$ cilia were indeed shorter than *NEK10*^{WT} cilia (Fig. 4c,d, $6.24 \pm 1.26\,\mu m$ versus $7.86 \pm 1.06\,\mu m$), providing at least a partial basis for ciliary transport failure based on biophysical models of mucociliary transport that include ciliary length as a critical parameter in force generation[26–28].

To explore the biochemical functions of NEK10 in airway epithelium, we next performed iron-enrichment proteomics[29] (LC–IMAC MS^2) to identify a set of phosphopeptides that were depleted upon *NEK10* inactivation in ALI cultures (Extended Data Fig. 5c). Gene ontology analysis[30,31] revealed that these depleted peptides were highly enriched in ciliary motility and axonemal assembly genes, suggesting that a large complement of ciliary proteins is dysregulated upon NEK10 loss (Extended Data Fig. 5d). To test this hypothesis directly, we analyzed the effects of *NEK10* deletion on a set of proteins previously identified by proteomics in airway cilia[32] and found a striking and highly significant depletion of such ciliary phosphopeptides (median $\log_2$[fold change] −1.06 (sgNEK10b), −0.771 (sgNEK10c), Fig. 4e). Notably, although we observed similar findings upon analysis of peptides that mapped to annotated PCD genes, we saw little to no depletion of peptides from non-PCD ciliopathy genes, consistent with a specific role for NEK10 in the regulation of motile ciliogenesis (Extended Data Fig. 5e,f). Peptides from virtually all classes of motile ciliary genes were depleted in *NEK10*^{KO} ALI cultures (Fig. 4f), including axonemal motors, intraflagellar transport components, central pair constituents, and ciliary length control proteins, indicating that diverse members of the ciliary proteome are directly or indirectly dysregulated upon *NEK10* loss and providing a data set for future efforts to dissect its target network.

In summary, we describe a novel human disease caused by NEK10 deficiency and characterized by pathologically short motile cilia, as evidenced by multiple orthogonal assays in physiologically-relevant human airway preparations. In light of the highly cell-type-restricted expression of *NEK10* in our own data and those of recently generated cell atlases[2,33,34], as well as the absence of extra-respiratory phenotypes in our patients, this gene does not appear to be essential for primary ciliogenesis in humans, as has been proposed previously[10], but instead probably specifically controls MCC function. Indeed, as the lengths of protozoan beating cilia[35] and flagella[36–38] are regulated by distant *NEK* homologs, analogous pathways likely operate in metazoan MCCs to tune ciliary function to physiological needs. Although the central role of NEK10 in the potentiation of mucociliary clearance is clear from our study, the mechanistic basis for this activity remains to be fully explained because our current proteomic data cannot distinguish unambiguously between direct phosphorylation effects and secondary protein abundance changes. We are optimistic that future work will clarify the full repertoire of direct and indirect NEK10 targets in ciliated cells.

In parallel with these scientific insights, our work has potential implications for the diagnosis and treatment of bronchiectasis. In particular, the identification of multiple kindreds with *NEK10* mutations in whom ciliary electron microscopy, nasal nitric oxide, and high-speed video microscopy findings are all essentially normal suggests that standard algorithms for ruling out PCD may fail to capture such patients and others with mechanistically similar motile ciliopathies. Indeed, because prior studies have suggested that ciliary shortening (for example, owing to smoking[26,39]) may have a role in impaired mucociliary clearance in vivo, our results suggest that this relatively subtle histological abnormality should be more regularly evaluated for patients with otherwise unexplained mucus clearance deficiencies, as it may be more common than is currently appreciated. Finally, because this report directly implicates a kinase mutation in ciliary dyskinesia to our knowledge for the first time, it opens the door to understanding new regulatory networks in ciliated cells and, based on this understanding, potentially to targeting this signaling axis in more common diseases of mucociliary clearance where promotion of mucociliary transport may be therapeutically beneficial[26,40].

Online content

Any methods, additional references, Nature Research reporting summaries, source data, extended data, supplementary information, acknowledgements, peer review information; details of author contributions and competing interests; and statements of data and code availability are available at https://doi.org/10.1038/s41591-019-0730-x.

Received: 11 April 2019; Accepted: 6 December 2019;
Published online: 20 January 2020

References

1. Tilley, A. E., Walters, M. S., Shaykhiev, R. & Crystal, R. G. Cilia dysfunction in lung disease. *Annu. Rev. Physiol.* **77**, 379–406 (2015).
2. Montoro, D. T. et al. A revised airway epithelial hierarchy includes CFTR-expressing ionocytes. *Nature* **560**, 319–324 (2018).
3. Gould, C. M., Freeman, A. F. & Olivier, K. N. Genetic causes of bronchiectasis. *Clin. Chest Med.* **33**, 249–263 (2012).
4. Zariwala, M. A., Knowles, M. R. & Omran, H. Genetic defects in ciliary structure and function. *Annu. Rev. Physiol.* **69**, 423–450 (2007).
5. *Online Mendelian Inheritance in Man, OMIM* (McKusick–Nathans Institute of Genetic Medicine, Johns Hopkins University, November 2019); https://www.omim.org/
6. Moniz, L., Dutt, P., Haider, N. & Stambolic, V. Nek family of kinases in cell cycle, checkpoint control and cancer. *Cell Div.* **6**, 18 (2011).
7. Thiel, C. et al. *NEK1* mutations cause short-rib polydactyly syndrome type Majewski. *Am. J. Hum. Genet.* **88**, 106–114 (2011).
8. Smith, L. A. et al. Development of polycystic kidney disease in juvenile cystic kidney mice: insights into pathogenesis, ciliary abnormalities, and common features with human disease. *J. Am. Soc. Nephrol.* **17**, 2821–2831 (2006).
9. Moniz, L. S. & Stambolic, V. Nek10 mediates G2/M cell cycle arrest and MEK autoactivation in response to UV irradiation. *Mol. Cell. Biol.* **31**, 30–42 (2011).
10. Porpora, M. et al. Counterregulation of cAMP-directed kinase activities controls ciliogenesis. *Nat. Commun.* **9**, 1224 (2018).
11. Fulcher, M. L., Gabriel, S., Burns, K. A., Yankaskas, J. R. & Randell, S. H. Well-differentiated human airway epithelial cell cultures. *Methods Mol. Med.* **107**, 183–206 (2005).
12. Knowles, M. R., Zariwala, M. & Leigh, M. Primary ciliary dyskinesia. *Clin. Chest Med.* **37**, 449–461 (2016).
13. Karczewski, K. J. et al. Variation across 141,456 human exomes and genomes reveals the spectrum of loss-of-function intolerance across human protein-coding genes. *bioRxivorg* **49**, 531210 (2019).
14. Ostrowski, L. E., Hutchins, J. R., Zakel, K. & O'Neal, W. K. Targeting expression of a transgene to the airway surface epithelium using a ciliated cell-specific promoter. *Mol. Ther.* **8**, 637–645 (2003).
15. Liu, L. et al. Method for quantitative study of airway functional microanatomy using micro-optical coherence tomography. *PLoS ONE* **8**, e54473 (2013).
16. Knowles, M. R., Daniels, L. A., Davis, S. D., Zariwala, M. A. & Leigh, M. W. Primary ciliary dyskinesia. Recent advances in diagnostics, genetics, and characterization of clinical disease. *Am. J. Respir. Crit. Care Med.* **188**, 913–922 (2013).
17. He, Y., Zeng, M. Y., Yang, D., Motro, B. & Nuñez, G. NEK7 is an essential mediator of NLRP3 activation downstream of potassium efflux. *Nature* **530**, 354–357 (2016).
18. Carrera, A. C., Alexandrov, K. & Roberts, T. M. The conserved lysine of the catalytic domain of protein kinases is actively involved in the phosphotransfer reaction and not required for anchoring ATP. *Proc. Natl Acad. Sci. USA* **90**, 442–446 (1993).
19. Moniz, L. *Characterization of NimA-related Kinase 10 (NEK10): A Role in Checkpoint Control*. PhD thesis, Univ. of Toronto (2010).
20. Richards, M. W. et al. An autoinhibitory tyrosine motif in the cell-cycle-regulated Nek7 kinase is released through binding of Nek9. *Mol. Cell* **36**, 560–570 (2009).
21. Doan, M. et al. Diagnostic potential of imaging flow cytometry. *Trends Biotechnol.* **36**, 649–652 (2018).
22. Wallmeier, J. et al. Mutations in *CCNO* result in congenital mucociliary clearance disorder with reduced generation of multiple motile cilia. *Nat. Genet.* **46**, 646–651 (2014).
23. Boon, M. et al. *MCIDAS* mutations result in a mucociliary clearance disorder with reduced generation of multiple motile cilia. *Nat. Commun.* **5**, 4418 (2014).
24. Vladar, E. K., Nayak, J. V., Milla, C. E. & Axelrod, J. D. Airway epithelial homeostasis and planar cell polarity signaling depend on multiciliated cell differentiation. *JCI Insight* **1**, 183 (2016).
25. Ostrowski, L. E. in *Cell Biology* 3rd edn, Vol. 2 (ed., Celis, J. E.) Ch. 14 (Elsevier, 2005).
26. Leopold, P. L., O'Mahony, M. J., Lian, X. J., Tilley, A. E., Harvey, B.-G. & Crystal, R. G. Smoking is associated with shortened airway cilia. *PLoS ONE* **4**, e8157 (2009).
27. Oltean, A., Schaffer, A. J., Bayly, P. V. & Brody, S. L. Quantifying ciliary dynamics during assembly reveals stepwise waveform maturation in airway cells. *Am. J. Respir. Cell Mol. Biol.* **59**, 511–522 (2018).
28. Bottier, M., Thomas, K. A., Dutcher, S. K. & Bayly, P. V. How does cilium length affect beating? *Biophys. J.* **116**, 1292–1304 (2019).
29. Block, H. et al. Immobilized-metal affinity chromatography (IMAC): a review. *Meth. Enzymol.* **463**, 439–473 (2009).
30. Ashburner, M. et al. Gene ontology: tool for the unification of biology. *Nat. Genet.* **25**, 25–29 (2000).
31. The Gene Ontology Consortium. The Gene Ontology Resource: 20 years and still GOing strong. *Nucleic Acids Res.* **47**, D330–D338 (2019).
32. Ostrowski, L. E. et al. A proteomic analysis of human cilia identification of novel components. *Mol. Cell Proteomics* **1**, 451–465 (2002).
33. Vieira Braga, F. A. et al. A cellular census of human lungs identifies novel cell states in health and in asthma. *Nat. Med.* **25**, 1153–1163 (2019).
34. Tabula Muris Consortium. et al. Single-cell transcriptomics of 20 mouse organs creates a *Tabula Muris*. *Nature* **562**, 367–372 (2018).
35. Wloga, D. et al. Members of the NIMA-related kinase family promote disassembly of cilia by multiple mechanisms. *Mol. Biol. Cell* **17**, 2799–2810 (2006).
36. Bradley, B. A. & Quarmby, L. M. A NIMA-related kinase, Cnk2p, regulates both flagellar length and cell size in *Chlamydomonas*. *J. Cell Sci.* **118**, 3317–3326 (2005).
37. Hilton, L. K., Gunawardane, K., Kim, J. W., Schwarz, M. C. & Quarmby, L. M. The kinases LF4 and CNK2 control ciliary length by feedback regulation of assembly and disassembly rates. *Curr. Biol.* **23**, 2208–2214 (2013).
38. Lin, H. et al. A NIMA-related kinase suppresses the flagellar instability associated with the loss of multiple axonemal structures. *PLoS Genet.* **11**, e1005508 (2015).
39. Hessel, J. et al. Intraflagellar transport gene expression associated with short cilia in smoking and COPD. *PLoS ONE* **9**, e85453 (2014).
40. Chen, Z.-G. et al. Aberrant epithelial remodeling with impairment of cilia architecture in non-cystic fibrosis bronchiectasis. *J. Thorac. Dis.* **10**, 1753–1764 (2018).

Methods

Whole exome sequencing and clinical phenotyping. Clinical whole exome sequencing was performed on kindreds 1–3 by the Molecular Diagnostics Laboratory of the King Faisal Specialist Hospital and Research Centre (KFSHRC). Exome enrichment was performed using the Agilent SureSelect Target Enrichment workflow before high-throughput sequencing on the Illumina HiSeq 2500 system. Greater than 30× coverage of 95% of the target regions was obtained for all samples. Exome sequences were mapped to the UCSC hg19 reference sequence with a custom pipeline and interrogated for variants using databases customized to Arab populations. Sequencing of proband siblings and additional kindreds was performed under a protocol approved by the KFSHRC Institutional Review Board (REC 2121053). Sequencing and analysis of kindred 4 were performed under a protocol approved by the University Children's Hospital Muenster Institutional Review Board (AZ 2015-104-f-S). Sequencing and analysis of kindred 5 were performed under protocols approved by the UNC Chapel Hill Institutional Review Board (05-2979 and 13-2348).

HBEC and ALI tissue culture. Control human samples were obtained from discarded lung allografts under a protocol approved by the Partners Human Research Committee (IRB 2012P001079). Samples from the proband were obtained at the time of bilateral lung transplantation under a protocol approved by the Partners Human Research Committee (IRB 2013P002332) and informed consent was obtained before organ explantation. Airway cells were obtained as described previously[41]. In brief, bronchial tube sections were rinsed in MEM supplemented with dithiothreitol and DNAse I before overnight incubation in MEM supplemented with pronase, DNAse I, antibiotics, and antifungals. Epithelial sheets were further dissociated with Accutase (Innovative Cell Technologies AT104) and plated into PneumaCult Ex-Plus expansion medium (StemCell Technologies 05040). All plates were pre-coated with sterile-filtered, laminin-rich conditioned medium (DMEM + 10% FBS) of the 804G rat bladder cell line to promote HBEC adhesion. HBECs were used between passages 2 and 5 for experiments and were dissociated for sub-culturing with TrypLE Select (Gibco 12563011). ALI cultures were established using 24-well (Corning 3470) or 6-well (Corning 3412) plates coated with 804G-conditioned medium. At confluence, apical medium was removed and basolateral medium was changed to PneumaCult-ALI (StemCell Technologies 05001) for 4 to 6 weeks of differentiation ('mature ALI'), except where stated otherwise in the text. Medium was exchanged every 48 h, and cultures were washed weekly with PBS buffer beginning on ALI day 14 on a plate shaker at 600 r.p.m. ×2.

qRT–PCR. Total RNA was extracted with Trizol reagent (Invitrogen) according to the manufacturer's protocol before first strand cDNA synthesis with the SuperScript VILO system (Invitrogen). qRT–PCR was performed using the PowerUp SYBR Green reagent (ABI) on an ABI QuantStudio 6 instrument. All analyses were performed with standard curve-based quantification and normalization to 18S ribosomal RNA abundance. A two-tailed Student's *t*-test was performed for analysis of statistical significance. qRT–PCR primer sequences are available in Supplementary Table 2 and were designed using Primer3Plus software to span exon–exon junctions in all cases.

Immunoblotting. Protein lysates were prepared in lysis buffer that contained 1% Triton X-100, 10 mM β-glycerol phosphate, 10 mM pyrophosphate, 40 mM HEPES pH 7.4, 2.5 mM $MgCl_2$, and one mini tablet of EDTA-free protease inhibitor (Roche cOmplete Mini, EDTA-free, product 11836170001) per 10 ml. Lysates were subjected to SDS–PAGE electrophoresis and transferred to polyvinylidene difluoride membranes before immunoblotting with the indicated antibodies. Primary antibodies and working dilutions were rabbit anti-NEK10 (Sigma HPA038941, lot R35857, 1:1,000), mouse anti-NEK10 (Sigma WH0152110M1, lot 09058-1C9, 1:1,000), rabbit anti-GAPDH (Abcam ab9485, 1:2,500), mouse anti-FLAG M2 (Sigma F1804, lot SLBS3530V, 1:1,000), rabbit anti-Raptor (Millipore 09-217, lot 3236353, 1:1,000), mouse anti-β-actin (Santa Cruz sc-47778, lot K1718, 1:1,000), and mouse anti-Ac-α-tubulin (Sigma T7451, 1:1,000). Secondary antibodies and dilutions were HRP-conjugated anti-rabbit IgG (Cell Signaling Technologies 7074, 1:3,000) and HRP-conjugated anti-mouse IgG (Cell Signaling Technologies 7076, 1:3,000).

***NEK10* cDNA cloning.** Total RNA was extracted with Trizol reagent according to the manufacturer's protocol before reverse transcription with the SuperScript IV system (Invitrogen) using oligo-dT priming. Full-length *NEK10* cDNAs were amplified with Platinum SuperFi polymerase (Invitrogen) and cloned into the pCR-Blunt II-TOPO vector (Invitrogen) according to the manufacturer's protocol, and individual clones were sequenced completely. Consensus control and $NEK10^{G>C}$ sequences cloned from each genotype were used for further experiments as indicated in the text. Cloning primers are available in Supplementary Table 2.

Linkage analysis. Genomic DNA was extracted from whole blood using a standard protocol. Genome-wide genotypes were obtained using an Affymetrix Axiom GWH-96 SNP Chip platform following the manufacturer's instructions. Blocks of homozygosity were identified using AutoSNPa[42]. Linkage analysis was performed on the single nucleotide polymorphism (SNP) genotypes using the Allegro component of easyLINKAGE software[43]. Statistical significance was assessed using a genome-wide logarithm of odds (LOD) score threshold of 3.3, which corresponded to a type I error rate of 5%.

Immunofluorescence microscopy. ALI samples were washed in PBS, fixed for 15 min in 4% paraformaldehyde (PFA), washed three times in PBS, and cut free from their plastic supports. For centrin staining only, samples were fixed in ice-cold methanol for 15 min at −20 °C but otherwise processed identically. ALI membranes were then blocked (5% donkey serum + 0.3% Triton X-100) for 1 h at room temperature (22 °C) before incubation with the indicated primary antibodies overnight at 37 °C in dilution buffer (1% BSA + 0.3% Triton X-100). Membranes were washed four times in wash buffer (PBS + 0.1% Triton X-100) before probing with fluorophore-conjugated secondary antibodies for 1 h at 37 °C in dilution buffer. DAPI was added to the secondary antibody solution for nuclear counterstaining. Membranes were washed four additional times in wash buffer and once in PBS before mounting in Fluoromount-G (Southern Biotech). Confocal images were obtained with an Olympus FV10i confocal laser-scanning microscope with a ×60 oil objective.

The following primary antibodies were used: mouse anti-Ac-α-tubulin, (gift from J. Rajagopal, Sigma T6793, 1:1,000), mouse anti-MUC5AC, (gift from J. Rajagopal, Thermo Fisher MS-145, lot 145p1709c, 1:500), goat anti-CCSP (gift from B. Stripp, no lot data (non-commercial), 1:5,000), chicken anti-KRT5, (gift from J. Rajagopal, Biolegend 905901, 1:500), rabbit anti-CETN1, (gift from I. Cheeseman, no lot data (non-commercial), 1:5,000), and rabbit anti-VANGL1, (gift from J. Rajagopal, Sigma HPA025235, lot c101664, 1:500). All secondary antibodies were Alexa Fluor conjugates used at 1:500 dilution (Life Technologies): goat anti-chicken 488 (A-11039, lot 1599396), donkey anti-mouse 488 (A-21202, lot TF271737), donkey anti-rabbit 488 (A-21206, lot TI271741), donkey anti-mouse 594 (R37115), and donkey anti-rabbit 594 (R37119, lot TI271728).

Assessment of SCGB1A1-, MUC5AC-, and Ac-α-tubulin-positive areas was performed using automated scripts for object segmentation in ImageJ with the FIJI implementation[44], and null hypothesis testing was performed using the two-tailed Student's *t*-test. The KRT5-positive area could not be quantified, as basal cells form an essentially contiguous layer. Centrin puncta were quantified using automated scripts in ImageJ/FIJI that counted local maxima within ciliated cells. Basal body density was then calculated by dividing total puncta by cell number. Source code for the scripts is available on request. Null hypothesis testing was performed using a two-tailed Student's *t*-test.

Lentivirus cloning, production, and HBEC infection. *NEK10*:eGFP and *FOXJ1*:eGFP vectors were generated by amplifying the respective promoter regions from human genomic DNA and replacing the existing cytomegalovirus promoter of the pLJM1 construct (Addgene 19319) using NEBuilder Gibson assembly (New England Biolabs). The putative *NEK10* promoter was identified as a conserved ~1.6 kb region bounding the *NEK10* transcription start site and harboring epigenetic marks consistent with promoter function. The *FOXJ1* promoter sequence was cloned using a previously described[14] region as a guide. Gibson assembly was also used to generate *FOXJ1*-promoter-driven lentiviral expression vectors by replacing the cytomegalovirus promoter of the pLJC2 vector (Addgene 87974). *NEK10* mutants were generated using a site-directed mutagenesis strategy followed by Gibson assembly into the aforementioned *FOXJ1*-driven expression vectors. Lentiviral vectors expressing Cas9–sgRNA (single guide RNA) were generated using the pLentiCRISPRv2 vector (Addgene 52961). In brief, guide RNAs that targeted *NEK10* or the *AAVS1* control locus were selected from our previously published[45] guide library (Addgene 1000000100), synthesized from annealed DNA oligonucleotides, cloned into BsmbI-digested pLentiCRISPRv2 vector, screened, and sequenced to confirm identity. Cloning primers are available in Supplementary Table 2.

Lentiviruses were produced as follows: HEK293T cells were transfected with lentiviral constructs and viral packaging plasmids psPAX2 (Addgene 12260) and pCMV-VSVG (Addgene 8454) using the X-tremeGene HP reagent (Sigma). Viral supernatants were collected and concentrated using the Lenti-X Concentrator system (Takara) before use for HBEC infection. Low-passage HBECs were infected with concentrated lentivirus and selected 48 h later with 1 μg ml^{-1} puromycin for an additional 48 h before ALI culture seeding.

FACS. Mature ALI cultures were washed with PBS and incubated in TrypLE Select (Gibco) for 1 h at 37 °C to liberate single cells. Cells were strained through a 70 μm cell strainer to remove clumps and debris, washed in 1× PBS, and resuspended in a buffer that contained 1% FBS, 1 mM EDTA, and 25 mM HEPES. Sorting was performed using a BD FACSAria instrument (BD Biosciences) running FACSDiva software, and analysis was performed using FlowJo (version 10) software. GFP+ cells were sorted after gating (Extended Data Fig. 2i) on viable (by exclusion of vital dye) singlets (by measurements of forward scatter and side scatter) and collected for RNA isolation in Trizol.

ALI live phase contrast imaging. Mature ALI transwells were moved from their media to glass-bottomed tissue culture dishes and imaged under ×40 objective magnification with phase contrast optics at 30 frames per s for a total of 300

frames using a Zeiss Axio Observer.Z1 inverted microscope. The resulting 8-bit monochrome videos were processed in ImageJ/FIJI as follows: each 300-frame stack was duplicated, and a new 299-frame stack (the 'difference stack') was generated by subtracting the $(n+1)$th frame from the nth frame. The mean intensity of every pixel in the difference stack was then calculated, and the resultant data were output to a single TIF file that visually represented the average pixel intensity change over the course of video, which was a surrogate for motion. This TIF file was pseudocolored using the 'fire' lookup table to yield the final processed images. Data collected in a single experimental imaging session are displayed with identical brightness and contrast thresholds to enable direct visual comparison between experimental conditions. Source code for the scripts is available on request. For quantification, mean intensities of the TIF files were extracted in ImageJ, normalized per imaging session, and reported as relative intensity levels. Null hypothesis testing was performed using a two-tailed Student's *t*-test.

Micro-optical coherence tomography. The μOCT measurements were performed and analyzed as described previously[15,46]. In brief, PCL depth and CBF were assessed directly using cross-sectional images of the airway epithelium with high resolution (~1 μm) and high acquisition speed (20,480 Hz A-line rate resulting in 40 frames per s at 512 A-lines per frame across a 1 mm lateral range). Quantitative analysis of images was performed in ImageJ/FIJI. To establish CBF, previously published custom code in Matlab (Mathworks) was used to quantify Fourier-transformed reflectance modulations of beating cilia. PCL depth was characterized directly by geometric measurement of the respective layers. For measurement of mucociliary transport, native mucus was washed away completely with PBS, and 0.5 μm polystyrene beads (Invitrogen F8813) were added to the apical ALI surface before imaging. Particle tracking was performed using MosaicSuite in ImageJ[47], and the resulting particle tracks were analyzed in Matlab. Particles included for analysis were within 90 μm of the epithelial surface, present for at least 20 frames (0.5 s), and had a velocity vector within 10° of horizontal. Hypothesis testing was performed using a Mann–Whitney *U*-test or, when it was necessary to control for environmental differences (temperature, humidity, etc.) and instrument changes between imaging sessions, by a linear mixed-effects model.

Imaging flow cytometry. Single cells were generated from mature ALI cultures as described above, fixed in 2% PFA, and resuspended in PBS before analysis on an ImageStream^X MkII instrument (Amnis). The gating strategy was as follows: starting with unclipped events using a centroid X gate, we obtained in-focus cells using a gradient root mean square gate. We next used a liberal area versus aspect ratio gate (R1) to exclude clumps, followed by an area versus GFP intensity plot to gate on GFP+ cells (R2), followed by a GFP morphology mask versus aspect ratio gate (R3) to exclude GFP doublets, followed by a final doublet removal step again gated on bright-field (R4). We finally gated on cells with a minimum mean pixel value of 45 in the GFP channel (R6). This strategy yielded 4,108 imaged single cells from *NEK10*^{WT} and 3,513 imaged single cells from *NEK10*$^{G>C}$ ALI samples. From this parent population of unclipped, singlet, in-focus GFP+ cells, we defined masks of whole cells and GFP+ cell bodies. The major axis difference was calculated by subtracting the major axis of the GFP mask from the whole-cell mask, and the area difference was calculated by subtracting the GFP mask area from the whole-cell mask area. Null hypothesis testing was performed using a two-tailed Student's *t*-test. Representative images centered on the medians of the indicated populations were selected for gallery images.

Clinical histopathology. Age-matched patients who had undergone pneumonectomy (patients 1–3) or lobectomy (patient 4) at Massachusetts General Hospital between 2018 and 2019 were identified and their H&E-stained clinical slides were photographed in compliance with IRB 2016P001475. Well-preserved and well-oriented airway tissue was photographed at ×400 magnification and processed identically for all panels.

SEM, STEM, and negative stain electron micropscopy. ALI cultures were washed in PBS, fixed in a solution of 2% PFA, 2.5% glutaraldehyde, and 0.1 M sodium cacodylate for 150 min at room temperature, fixed in fresh fixative for 1 h at 4 °C, washed three times in 0.1 M sodium cacodylate, dehydrated, and then sputter coated with gold. SEM images were acquired on a Zeiss Crossbeam 540 dual-beam scanning microscope using secondary electron imaging. Scanning transmission electron microscopy (STEM) samples were prepared identically before resin embedding, ultrathin section cutting, and imaging on a Zeiss Crossbeam 540 operating in STEM mode. For negative stain electron microscopy, samples were adsorbed onto 200 mesh carbon film copper grids for 1 min, rinsed for 30 s with distilled water, then stained with 2% uranyl acetate for 1 min, again washed with distilled water, and imaged on a Zeiss Crossbeam 540. Resultant micrographs were analyzed and individual cilia measured in ImageJ/FIJI; null hypothesis testing was performed using a two-tailed Student's *t*-test.

Ciliary isolation. Cilia were purified according to a previously published protocol with minor modifications[25]. Mature ALI cultures were washed three times in PBS before the addition of pre-chilled deciliation buffer (10 mM Tris pH 7.5, 50 mM NaCl, 10 mM $CaCl_2$, 1 mM EDTA, 7 mM β-mercaptoethanol, 0.1% Triton X-100, 1× Roche cOmplete Mini Protease Inhibitor Cocktail) and 1 min of vigorous rocking at 4 °C. Supernatants, which contained cilia, were removed to pre-chilled 1.5 ml tubes, and a second aliquot of deciliation buffer was applied for 1 min. Supernatants were then pooled and centrifuged for 1 min at 1,000*g* to pellet debris. Supernatants were removed carefully and centrifuged for 5 min at 12,000*g* to pellet axonemes. Ciliary preparations were resuspended in chilled resuspension buffer (300 mM HEPES pH 7.3, 250 mM NaCl, 50 mM $MgSO_4$, 10 mM EGTA, 1 mM EDTA, 10 mM dithiothreitol, 1× Roche cOmplete Mini Protease Inhibitor Cocktail) before use for electron microscopy or immunoblotting. De-ciliated ALI cultures were collected in lysis buffer (composition as above) and used for immunoblotting.

Phosphoproteomics and analysis. ALI cultures were grown to maturity, washed in PBS, and lysed in urea lysis buffer that contained 20 mM HEPES (pH 8.0), 9.0 M urea, 1 mM sodium orthovanadate (activated), 2.5 mM sodium pyrophosphate, and 1 mM ß-glycerol-phosphate. Lysates were protease-digested before phosphopeptide enrichment using immobilized metal ion affinity chromatography (Fe-IMAC). Eluted peptides were then subjected to liquid chromatography–tandem mass spectroscopy (LC–MS/MS) analysis using a Thermo Scientific Orbitrap Fusion Lumos mass spectrometer (electrospray ionization–higher-energy C-trap dissociation), and the resulting spectra were analyzed with the Thermo Scientific Proteome Discoverer implementation of the SEQUEST algorithm[48]. Each biological sample was run in duplicate injections. Searches were performed against the most recent update of the Uniprot *Homo sapiens* database with a mass accuracy of ±50 ppm for precursor ions and 0.02 Da for product ions. Results were filtered with a mass accuracy of ±5 ppm for precursor ions and the presence of the intended motif. This dataset yielded 56,540 redundant modified peptide assignments to 14,805 modified sites. Data were normalized by median offset correction based on all the relative abundance values in the data set and were expressed as log2[fold change] for analysis. Publicly available data sets were used to establish gene lists for the motile ciliary proteome[32], PCD genes[12] (Online Mendelian Inheritance in Man, MIM Number 244400)[5], non-PCD ciliopathy genes[49], axonemal dyneins and assembly factors ('Dyneins, axonemal' and 'Axonemal dynein assembly factors' sets from the HUGO Gene Nomenclature Committee, HGNC), kinesins (HGNC set 'Kinesins'), intraflagellar transport[50], radial spoke apparatus (HGNC RSPH gene family), central pair complex[51–53], and ciliary length control[54–60]. Gene ontology (GO) analysis was performed with published methods[30,31] using the PANTHER overrepresentation test against the GO Ontology database (2019-10-08 release) and the 'GO Biological Process Complete' annotation data set with publicly available online interface.

Statistics and reproducibility. Fig. 1: **d**, Two-tailed homoscedastic Student's *t*-test. $P=0.77$, $P=0.65$, and $P=0.99$ for comparisons of 5′, 3′, and upstream amplicons, respectively. Extended Data Fig. 2: **e**,**f**, Two-tailed homoscedastic Student's *t*-test. $P=0.14$, $P=0.21$, and $P=0.80$ for comparisons of Scgb1a1, Muc5ac, and Ac-α-tubulin, respectively. Fig. 2: **d**, Linear mixed-effects model (fixed effect, MCT; random effect, μOCT instrument session). $P=0.0252$. **e**, Linear mixed-effects model (fixed effect, PCL; random effect, μOCT instrument session). $P=0.0059$. **g**, Mann–Whitney *U*-test. All *P* values <0.0001 (minimum calculable by software). **h**, Mann–Whitney *U*-test. $P=0.0286$, $P=0.0159$, and $P=0.0095$ for sgNEK10a, sgNEK10b, and sgNEK10c, respectively. **i**, Mann–Whitney *U*-test. $P=0.0086$, $P=0.8967$, and $P<0.0001$ for *NEK10*^{WT}, *NEK10*^{K548R}, and *NEK10*^{S684D}, respectively. Extended Data Fig. 3: **a**, Two-tailed homoscedastic Student's *t*-test. $P=0.00048$. **c**, Linear mixed-effects model (fixed effect, CBF; random effect, μOCT instrument session). $P=0.1109$. **e**, Two-tailed homoscedastic Student's *t*-test. $P=0.0085$, $P=0.0006$, and $P=0.0014$ for sgNEK10a, sgNEK10b, and sgNEK10c, respectively. **f**, Mann–Whitney *U*-test. $P=0.0535$, $P=0.3947$, and $P=0.0112$ for sgNEK10a, sgNEK10b, and sgNEK10c, respectively. **h**, Two-tailed homoscedastic Student's *t*-test. $P=0.1374$, $P=0.4176$, $P=0.1688$, and $P=0.0220$ for *NEK10*^{WT}, *NEK10*^{K548R}, *NEK10*^{Y590A}, and *NEK10*^{S684D}, respectively. **j**, Mann–Whitney *U*-test. $P=0.3429$, $P=0.4857$, and $P=0.8857$ for *NEK10*^{WT}, *NEK10*^{K548R}, and *NEK10*^{S684D}, respectively. Fig. 3: **b**, Two-tailed homoscedastic Student's *t*-test. $P=1.802\times10^{-124}$. **c**, Two-tailed homoscedastic Student's *t*-test. $P=0.0000$ (minimum calculable by Microsoft Excel). Fig. 4: **d**, Two-tailed homoscedastic Student's *t*-test. $P=3.005\times10^{-19}$. Extended Data Fig. 5: **d**, Fisher's Exact test with false discovery rates listed for multiple hypothesis correction. *P* values are given in the table within the figure.

Reporting Summary. Further information on research design is available in the Nature Research Reporting Summary linked to this article.

Data availability

Sequence data that support the findings of this study have been deposited in NCBI GenBank under accession numbers MK806425 and MK806426. The mass spectrometry proteomics data have been deposited to the ProteomeXchange Consortium through the PRIDE partner repository with the dataset identifier PXD016600[61]. Plasmids pLRC1-NEK10p:NEK10-3XFLAG and pLRC1-FOXJ1p:NEK10-3XFLAG are available for review and distribution through Addgene (plasmid numbers 137030 and 137031). All other data and computer code are provided within the paper or in the Supplementary information. Raw data for

statistical tests (.xlsx files) and uncropped immunoblots that correspond to to Figs. 1–4 and Extended Data Figs. 2,3,5 (.pdf files) are provided.

References

41. Neuberger, T., Burton, B., Clark, H. & Van Goor, F. Use of primary cultures of human bronchial epithelial cells isolated from cystic fibrosis patients for the pre-clinical testing of CFTR modulators. *Methods Mol. Biol.* **741**, 39–54 (2011).
42. Carr, I. M. et al. Interactive visual analysis of SNP data for rapid autozygosity mapping in consanguineous families. *Hum. Mutat.* **27**, 1041–1046 (2006).
43. Hoffmann, K. & Lindner, T. H. easyLINKAGE-Plus—automated linkage analyses using large-scale SNP data. *Bioinformatics* **21**, 3565–3567 (2005).
44. Schindelin, J. et al. Fiji: an open-source platform for biological-image analysis. *Nat. Methods* **9**, 676–682 (2012).
45. Wang, T. et al. Identification and characterization of essential genes in the human genome. *Science* **350**, 1096–1101 (2015).
46. Liu, L. et al. Imaging the subcellular structure of human coronary atherosclerosis using micro-optical coherence tomography. *Nat. Med.* **17**, 1010–1014 (2011).
47. Sbalzarini, I. F. & Koumoutsakos, P. Feature point tracking and trajectory analysis for video imaging in cell biology. *J. Struct. Biol.* **151**, 182–195 (2005).
48. Eng, J. K., McCormack, A. L. & Yates, J. R. An approach to correlate tandem mass spectral data of peptides with amino acid sequences in a protein database. *J. Am. Soc. Mass Spectrom.* **5**, 976–989 (1994).
49. Reiter, J. F. & Leroux, M. R. Genes and molecular pathways underpinning ciliopathies. *Nat. Rev. Mol. Cell Biol.* **18**, 533–547 (2017).
50. Ishikawa, H. & Marshall, W. F. Ciliogenesis: building the cell's antenna. *Nat. Rev. Mol. Cell Biol.* **12**, 222–234 (2011).
51. Teves, M. E., Nagarkatti-Gude, D. R., Zhang, Z. & Strauss, J. F. Mammalian axoneme central pair complex proteins: broader roles revealed by gene knockout phenotypes. *Cytoskeleton* **73**, 3–22 (2016).
52. Osinka, A. et al. Ciliary proteins: filling the gaps. Recent advances in deciphering the protein composition of motile ciliary complexes. *Cells* **8**, 730 (2019).
53. Zhao, L., Hou, Y., Picariello, T., Craige, B. & Witman, G. B. Proteome of the central apparatus of a ciliary axoneme. *J. Cell Biol.* **218**, 2051–2070 (2019).
54. Satish Tammana, T. V., Tammana, D., Diener, D. R. & Rosenbaum, J. Centrosomal protein CEP104 (*Chlamydomonas* FAP256) moves to the ciliary tip during ciliary assembly. *J. Cell Sci.* **126**, 5018–5029 (2013).
55. Niwa, S. et al. KIF19A is a microtubule-depolymerizing kinesin for ciliary length control. *Dev. Cell* **23**, 1167–1175 (2012).
56. Lai, C. K. et al. Functional characterization of putative cilia genes by high-content analysis. *Mol. Biol. Cell* **22**, 1104–1119 (2011).
57. Vasudevan, K. K. et al. Kinesin-13 regulates the quantity and quality of tubulin inside cilia. *Mol. Biol. Cell* **26**, 478–494 (2015).
58. Piao, T. et al. A microtubule depolymerizing kinesin functions during both flagellar disassembly and flagellar assembly in *Chlamydomonas*. *Proc. Natl Acad. Sci. USA* **106**, 4713–4718 (2009).
59. Wang, L. et al. Flagellar regeneration requires cytoplasmic microtubule depolymerization and kinesin-13. *J. Cell Sci.* **126**, 1531–1540 (2013).
60. Broekhuis, J. R., Verhey, K. J. & Jansen, G. Regulation of cilium length and intraflagellar transport by the RCK-kinases ICK and MOK in renal epithelial cells. *PLoS ONE* **9**, e108470 (2014).
61. Perez-Riverol, Y. et al. The PRIDE database and related tools and resources in 2019: improving support for quantification data. *Nucleic Acids Res.* **47**, D442–D450 (2019).

Acknowledgements

We are grateful to the patients and family members who participated in this research. We thank J. Rajagopal for advice and reagents, B. Stripp (Cedars-Sinai) and I. Cheeseman (Whitehead Institute for Biomedical Research) for antibodies, the Peterson (1957) Nanotechnology Materials Core Facility at the Koch Institute for electron microscopy services, S. Mordecai for advice and assistance with IFC, H. Zheng for assistance with statistical methods, M. Mino-Kenudson for pulmonary pathology assistance, KFSHRC genotyping and sequencing core facilities for technical help, M. Manion and the Primary Ciliary Dyskinesia Foundation for support, L. Ostrowski for assistance with ciliary motility studies, K. Sullivan and N. Capps for patient coordination and specimen collection, V. Madden, J. Stonebraker, R. Pace, and K. Burns for technical assistance, H. Dang and H. Namkoong for bioinformatics assistance, and A. Lee and members of the Sabatini laboratory for critical reading of the manuscript. This work was supported by grants from the National Institutes of Health: T32HL116275 (R.R.C.), T32CA009216 (M.S.T.), U54HL096458 and UL1TR000083 (M.R.K., M.A.Z., M.L.D., and P.R.S.), R01HL071798 (M.R.K., M.L.D., and M.A.Z.), R01HL117836-01 (M.R.K., M.L.D., and M.A.Z.), R01CA129105 and R37AI047389 (D.M.S.). Additional funding support was provided by the Massachusetts General Hospital Department of Medicine Pathways program (R.R.C.) and by the King Salman Center for Disability Research and the Saudi Human Genome Program (F.S.A.). The Amnis ImageStream^X Mk II was purchased using a National Institutes of Health Shared Instrumentation Grant 1S10OD012027-01A1 to Massachusetts General Hospital. D.M.S. is an investigator at the Howard Hughes Medical Institute and an American Cancer Society Research Professor.

Author contributions

R.R.C. initiated the project, phenotyped the index proband, designed and performed all the experiments except as noted, analyzed the data, prepared the figures, and wrote the manuscript. D.T.M. assisted with the design and performance of the cell culture, IFM, and FACS experiments, analyzed the data, and edited the manuscript. H.M.L. performed the μOCT experiments, analyzed the data, and prepared the figures. J.Y. assisted with molecular cloning, site-directed mutagenesis, and cell culture, and edited the manuscript. H.E.S. performed the whole exome sequencing and linkage analysis on kindreds 1–3. M.S.T. acquired the clinical histopathology images and prepared the figures. G.W.D. performed the sequencing, molecular biology, and high-speed video microscopy (HSVM) analysis on kindred 4. M.A.Z. led the molecular analysis of kindred 5. J.C. performed and interpreted the kindred 5 ciliary electron microscopy and HSVM. M.L.D. identified the kindred 5 patients and provided clinical data. P.R.S. performed the HSVM. K.E.B. and L.P.H. assisted with the acquisition of proband 1 clinical samples. I.A. identified bronchiectasis kindreds 2 and 3. E.M.F. assisted with the analysis of the phosphoproteomics data. V.V. assisted with the IFM experiments, analyzed the data, and edited the manuscript. H.O. supervised and led the kindred 4 analyses. M.R.K. supervised and led the kindred 5 molecular analysis and clinical phenotyping. G.J.T. supervised the μOCT experiments and analyzed the data. F.S.A. supervised the whole exome sequencing and linkage analysis of kindreds 1–3, analyzed the genetics data, and edited the manuscript. D.M.S. supervised the project, designed the experiments, and edited the manuscript.

Competing interests

Massachusetts General Hospital, the Whitehead Institute for Biomedical Research, and the Massachusetts Institute of Technology are in the process of filing a provisional patent application covering the therapeutic augmentation of NEK10 signaling in disorders of mucociliary clearance (R.R.C. and D.M.S., inventors). All other authors have no competing interests.

Additional information

Extended data is available for this paper at https://doi.org/10.1038/s41591-019-0730-x.

Supplementary information is available for this paper at https://doi.org/10.1038/s41591-019-0730-x.

Correspondence and requests for materials should be addressed to R.R.C. or F.S.A.

Peer review information Kate Gao was the primary editor on this article and managed its editorial process and peer review in collaboration with the rest of the editorial team.

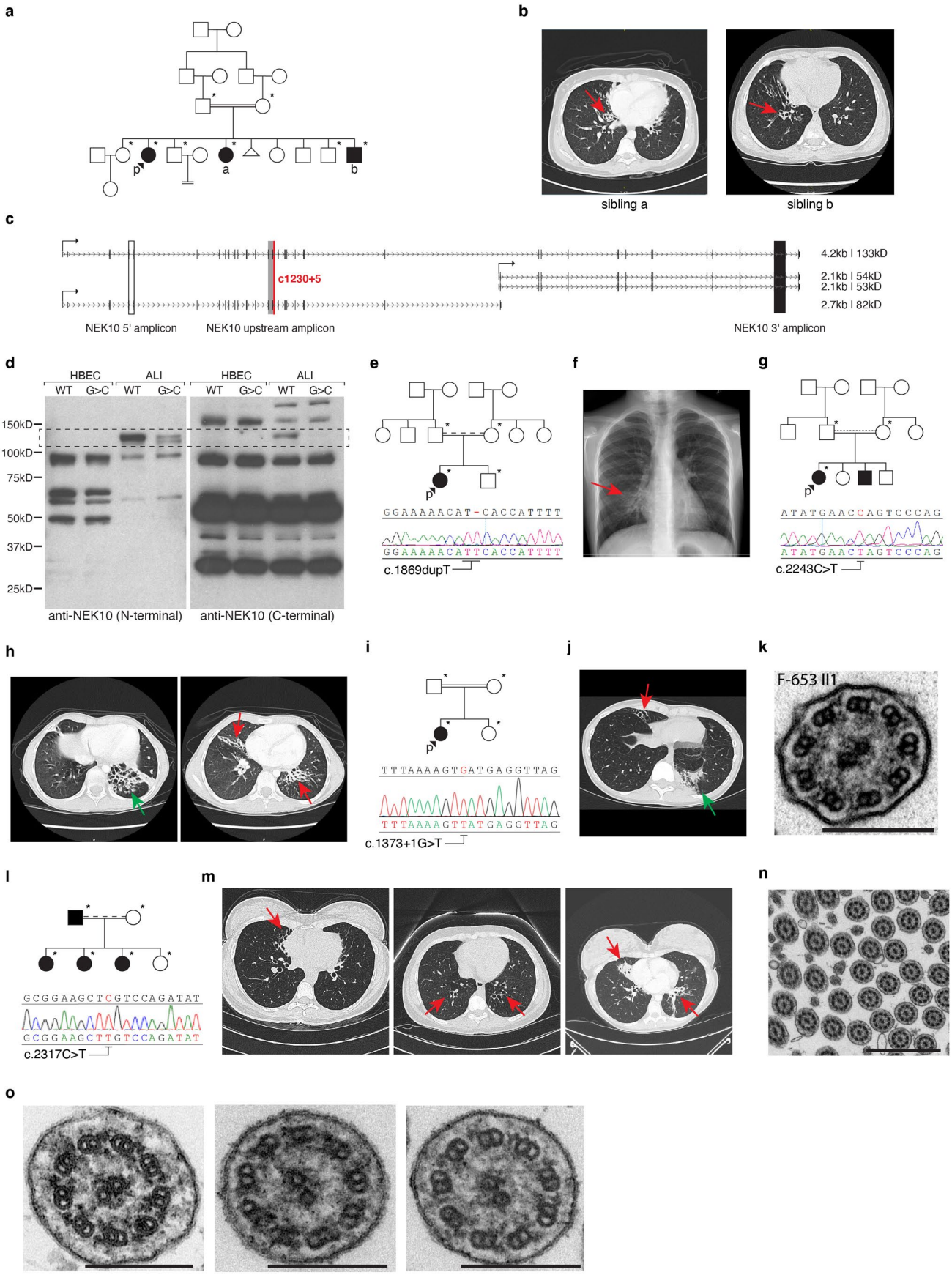

Extended Data Fig. 1 | See next page for caption.

Extended Data Fig. 1 | Recurrent *NEK10* mutations in familial bronchiectasis. a, Pedigree indicating affected siblings (filled), proband ('p'), and subjects from whom genomic DNA was available for analysis (asterisks). **b**, Chest CT of siblings 'a' and 'b' from panel (**a**), with arrows indicating regions of bronchiectatic lung. **c**, RefSeq-annotated *NEK10* variants annotated with transcription start sites, transcript sizes, predicted protein molecular weights, and exon–exon junctions assayed by qRT–PCR in Fig. 1d. **d**, Immunoblotting against indicated NEK10 epitopes, representative of three experiments. HBEC bands are non-specific. Full-length 133 kDa NEK10 protein is indicated with a dashed box. **e**, Pedigree of kindred 2. Asterisks denote family members from whom genomic DNA was available, the dashed line indicates consanguinity by shared tribal ancestry, and the Sanger sequencing trace confirms c.1869dupT. **f**, Chest radiograph of proband 2, with arrow highlighting bronchiectasis. **g**, Pedigree of kindred 3. The dashed line indicates consanguinity by shared geographical ancestry, and the Sanger sequencing trace confirms c.2243C>T. **h**, CT from proband 3 demonstrating cystic (green arrow) and cylindrical (red arrow) bronchiectasis. **i**, Pedigree of kindred 4. The Sanger sequencing trace confirms c.1371+1G>T. **j**, CT from proband 4 indicating right middle lobe (red arrow) and left lower lobe (green arrow) bronchiectasis. **k**, Proband 4 nasal biopsy TEM demonstrating normal radial ciliary ultrastructure. Scale bar, 200 nm. **l**, Pedigree of kindred 5. The dashed line indicates consanguinity by shared tribal ancestry, and the Sanger sequencing trace confirms c.2317C>T. **m**, CTs of affected siblings in (**l**), demonstrating bronchiectasis. **n**–**o**, Nasal biopsy TEM of affected siblings in (**l**). Scale bars, 1 μm (**n**) and 200 nm (**o**).

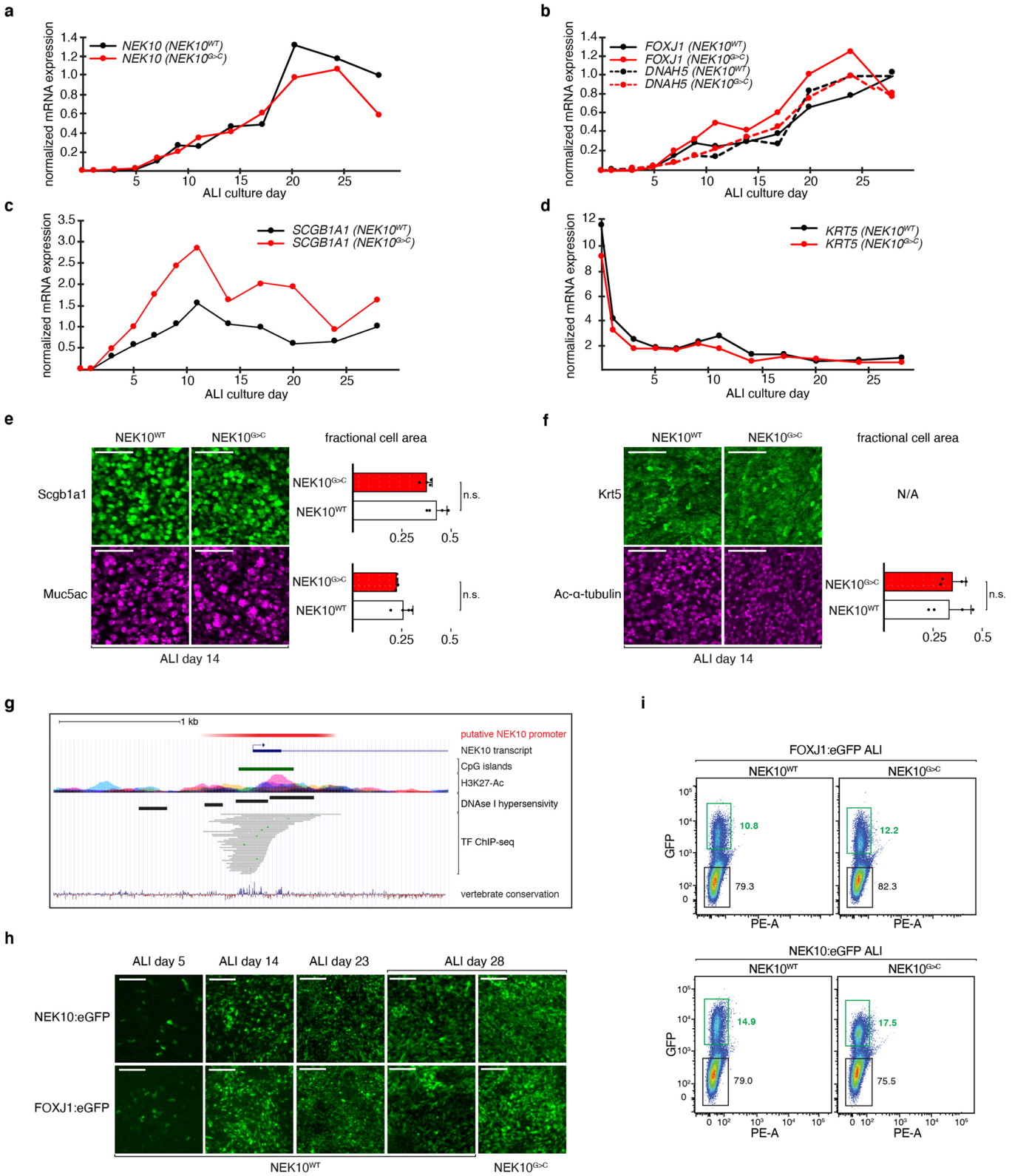

Extended Data Fig. 2 | *NEK10* loss does not detectably alter airway epithelial differentiation. a, 18S rRNA-normalized relative *NEK10* expression during ALI differentiation. $n=1$ ALI culture per time point. **b**–**d**, 18S rRNA-normalized relative expression of ciliated cell markers *FOXJ1* and *DNAH5* (**b**), secretory cell marker *SCGB1A1* (**c**), and basal cell marker *KRT5* (**d**). $n=1$ ALI culture per time point. **e**,**f**, Whole-mount immunofluorescence microscopy against SCGB1A1 (**e**, upper panel), goblet cell marker MUC5AC (**e**, lower panel), KRT5 (**f**, upper panel), and ciliated cell marker Ac-α-tubulin (**f**, lower panel). Scale bars, 100 µm. Bar graphs indicate the fraction of the surface epithelium occupied by marker-positive cells. $n=4$ per condition, representative of 6 ALI differentiations. Mean ± s.d. **g**, Schematic depiction of bioinformatic *NEK10* promoter (red) identification using the indicated UCSC genome browser hg19 tracks: CpG islands, H3K27-Ac, DNAse I hypersensitivity clusters, and transcription factor chromatin immunoprecipitation sequencing (ChIP-seq). **h**, Live GFP imaging of ALI cultures of the indicated genotypes and maturity, representative of three independent ALI differentiations. Scale bars, 200 µm. **i**, Gating strategy for FACS sorting of GFP-labeled ALI cultures. Numbers indicate the percentage of gated cells per population.

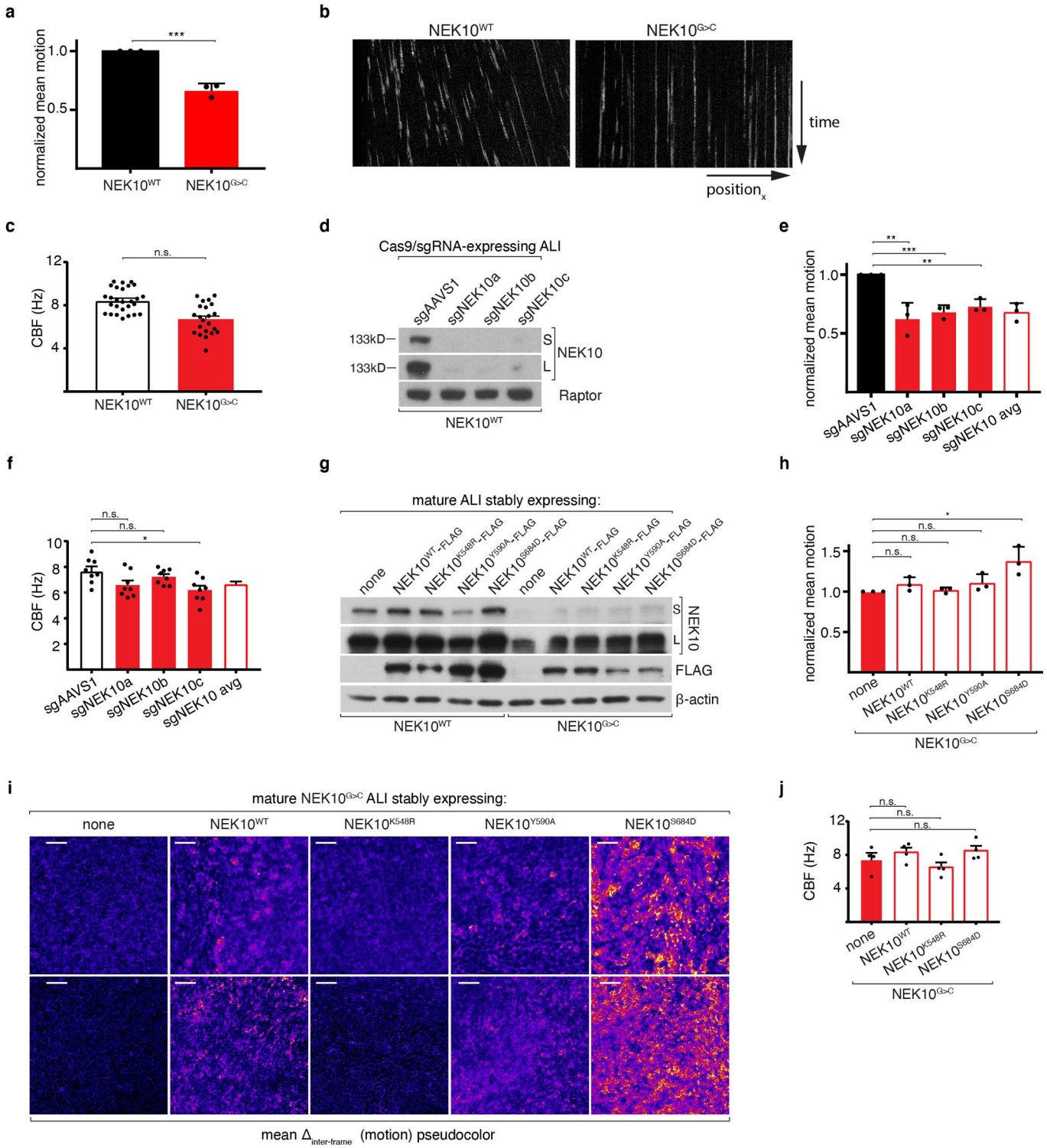

Extended Data Fig. 3 | Functional consequences of NEK10 activity manipulation. a, Quantification of analysis in Fig. 2c. Mean ± s.d. **b**, Kymographs of μOCT-based particle tracking from mature ALI cultures, representative of three independent ALI differentiations. **c**, CBF (μOCT) of mature ALI cultures of the indicated genotypes. $n = 27$ for *NEK10*^{WT} and $n = 22$ for *NEK10*$^{G>C}$, pooled from three independent ALI differentiations. Mean ± s.e.m. **d**, Immunoblotting of mature ALI lysates after CRISPR–Cas9-mediated gene editing with the indicated sgRNAs, representative of two experiments. Short (S) versus long (L) exposures are indicated. **e**, Quantification of analysis in Fig. 2f. Mean ± s.d. **f**, CBF of mature ALI cultures edited with the indicated sgRNAs, $n = 8$ per condition pooled from three independent ALI differentiations. Mean ± s.e.m. **g**, Immunoblotting of mature ALI lysates transduced with the indicated cDNAs, representative of 2 experiments. Short (S) versus long (L) exposures are indicated. **h**, Quantification of analysis in Fig. 2i. Mean ± s.d. **i**, Pseudocolored video microscopy of mature ALI cultures transduced with the indicated cDNAs. Representative fields from three independent ALI differentiations are shown. Scale bars, 50 μm. **j**, CBF of mature ALI cultures transduced with the indicated cDNAs. $n = 4$ per condition, pooled from three independent ALI differentiations. Mean ± s.e.m. $^{*}P \leq 0.05$, $^{**}P \leq 0.01$, $^{****}P \leq 0.0001$.

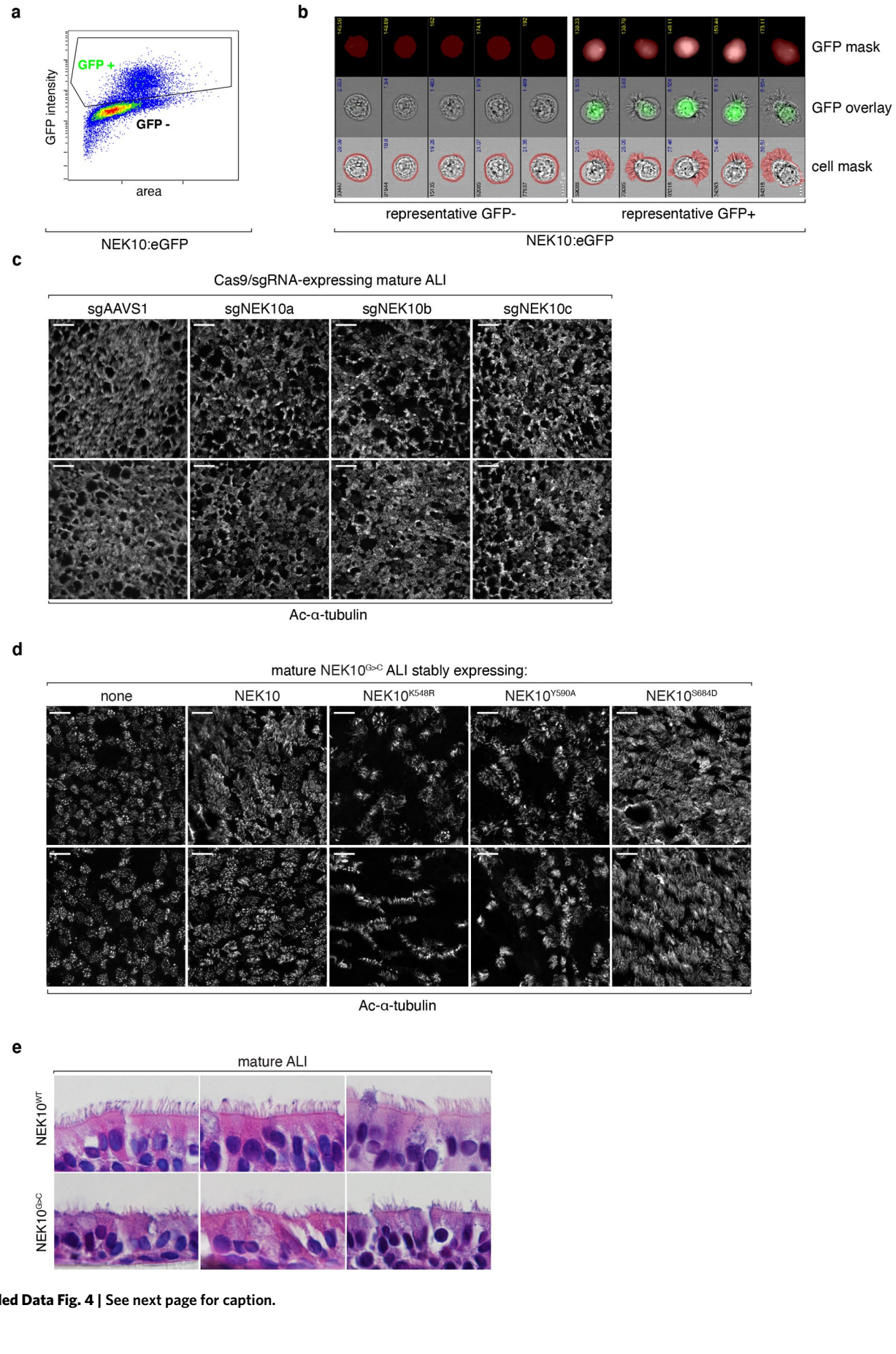

Extended Data Fig. 4 | See next page for caption.

Extended Data Fig. 4 | Experimental manipulation of NEK10 activity alters ciliated cell morphology. a, Gating strategy for IFC analysis of MCCs. **b**, Representative images and masking data of cells in (**a**), demonstrating the ability to generate single *NEK10*:eGFP+ ciliated cells for analysis. **c**, Confocal MIPs of mature ALI cultures edited with the indicated sgRNAs after IFM against Ac-α-tubulin, representative of two independent ALI differentiations. Scale bars, 25 μm. **d**, Confocal MIPs of mature ALI cultures transduced with the indicated cDNAs after IFM against Ac-α-tubulin, representative of two independent ALI differentiations. Scale bars, 25 μm. **e**, H&E stained mature ALI samples of the indicated genotypes after sectioning orthogonal to the epithelial surface, representative of three independent ALI differentiations.

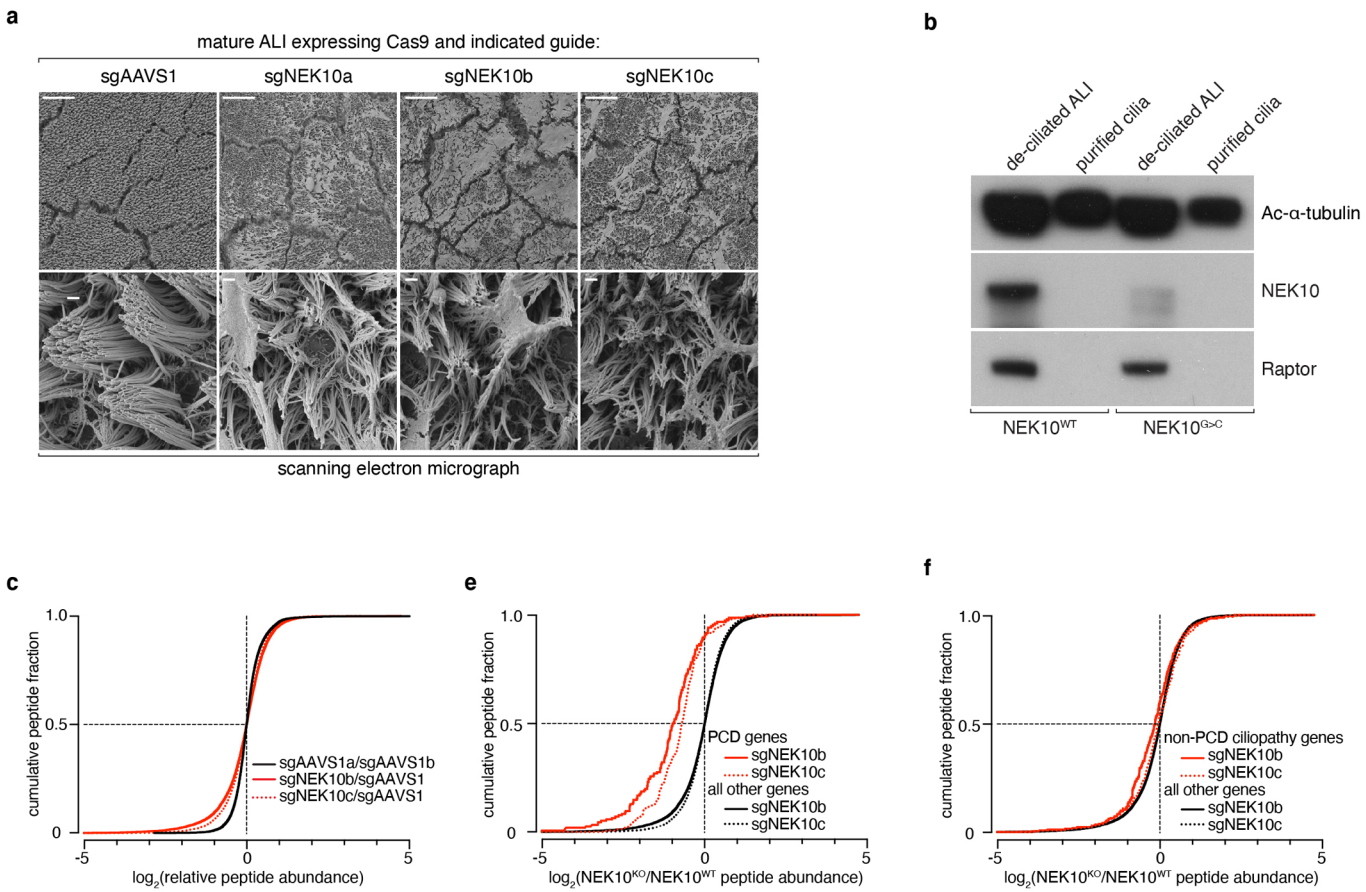

d

GO biological process	fold enrichment	p-value	FDR
cilium movement involved in cell motility (GO:0060294)	9.40	1.36E-04	3.82E-02
axoneme assembly (GO:0035082)	5.49	2.13E-08	4.56E-05
microtubule bundle formation (GO:0001578)	4.70	2.55E-09	1.37E-05
cilium movement (GO:0003341)	4.70	2.49E-06	1.90E-03
cilium-dependent cell motility (GO:0060285)	4.41	1.79E-05	1.13E-02
cilium or flagellum-dependent cell motility (GO:0001539)	4.41	1.79E-05	1.06E-02
microtubule-based movement (GO:0007018)	2.75	5.99E-07	4.93E-04
cilium organization (GO:0044782)	2.46	1.79E-07	2.13E-04
microtubule cytoskeleton organization (GO:0000226)	2.37	5.10E-08	7.80E-05
cilium assembly (GO:0060271)	2.32	3.33E-06	2.38E-03
microtubule-based process (GO:0007017)	2.26	2.33E-09	2.49E-05
plasma membrane bounded cell projection assembly (GO:0120031)	1.93	1.12E-04	3.43E-02
organelle assembly (GO:0070925)	1.92	1.10E-05	7.34E-03
cell projection assembly (GO:0030031)	1.92	1.24E-04	3.70E-02
unclassified (UNCLASSIFIED)	1.81	2.80E-05	1.36E-02
cytoskeleton organization (GO:0007010)	1.65	1.87E-05	1.06E-02

Extended Data Fig. 5 | Structural and proteomic abnormalities in NEK10-deficient airway epithelium. a, SEMs of mature ALI cultures edited with the indicated sgRNAs, representative of two independent ALI differentiations. Scale bars, 100 μm (upper panels) and 1 μm (lower panels). **b**, Immunoblotting against the indicated proteins from lysates generated from purified cilia (lanes 2 and 4) or remaining de-ciliated mature ALI cultures (lanes 1 and 3), representative of two experiments. **c**, Cumulative distribution of phosphopeptides by log2[fold change] between indicated conditions. The solid (sgNEK10b) and dashed (sgNEK10c) red lines illustrate the population of depleted phosphopeptides upon *NEK10* deletion. **d**, Table of GO classes enriched among genes ($n = 395$) whose peptides are depleted >1.5 fold $\log_2$[fold change] after targeting with sgNEK10b. The enrichment levels, *P* values, and false discovery rates are indicated. **e**, Cumulative distribution of phosphopeptides by $\log_2$[fold change]. Previously validated PCD proteins are in red and all other detected proteins are in black, as in Fig. 4e. **f**, Cumulative distribution of phosphopeptides by log2[fold change]. Previously validated non-PCD ciliopathy proteins are in red and all other detected proteins are in black, as in Fig. 4e.